JGR Atmospheres

RESEARCH ARTICLE
10.1029/2023JD038844

Application of a Three-Dimensional Coupled Hydrodynamic-Ice Model to Assess Spatiotemporal Variations in Ice Cover and Underlying Mechanisms in Lake Nam Co, Tibetan Plateau, 2007–2017

Yang Wu[1,2], Anning Huang[2,3], Youyu Lu[4], Ayumi Fujisaki-Manome[5], Zhiqi Zhang[6], Xianglin Dai[7], and Yu Wang[2]

[1]Nanjing Joint Institute for Atmospheric Sciences, Nanjing, China, [2]School of Atmospheric Sciences, Nanjing University, Nanjing, China, [3]Qinghai Lake Comprehensive Observation Research Station, Chinese Academy of Sciences, Gangcha, China, [4]Fisheries and Oceans Canada, Bedford Institute of Oceanography, Dartmouth, NS, Canada, [5]Cooperative Institute for Great Lakes Research, University of Michigan, Ann Arbor, MI, USA, [6]Shanghai Climate Center, Shanghai Meteorological Bureau, Shanghai, China, [7]Zhejiang Institute of Meteorological Sciences, Zhejiang Meteorological Bureau, Hangzhou, China

Abstract A three-dimensional lake-ice coupled model is used to investigate the space-time variations of ice and underlying mechanisms in Lake Nam Co (LNC), the third largest lake over Tibetan Plateau (TP), during 2007–2017. The model reasonably reproduces the in situ measured ice thickness and water temperature profile, and satellite retrieved ice coverage and lake surface temperature. Seasonally, the lake ice first forms in the eastern basin during early January, expands from east to west during January and February, covers nearly the entire LNC in March, starts melting from west to east in April, and eventually disappears in May. The eastward drift of thin ice throughout the ice-covered phase and the eastward water heat transport during the ice melting phase are key factors to determine the spatial variation of ice and freeze-thaw processes. A multiple linear regression analysis confirms that the eastward drift of thin ice can be mostly attributed to the prevailing westerly. During 2007–2017, ice volume, duration, ice-on and ice-off dates show significant interannual variations, and they are highly correlated with the surface air temperature (T_{2m}) averaged over January-March, from the preceding December to May, in December and over March–May, respectively, suggesting the "cumulative effects" of T_{2m}. Seasonal and interannual variations of ice drift are attributed to the combined effects of wind and ice volume variations. Sensitivity analysis further points out the important impacts of ice on the lake temperature and circulation structure in winter and spring, hence the necessity of hydrodynamic-ice coupled models in large TP lakes.

Plain Language Summary The space-time variations of ice play fundamental roles in controlling a wide range of physical and biogeochemical processes within lakes, as well as the regional climate, mainly by modulating the lake-air interactions. In this study, we use a three-dimensional lake-ice coupled model to investigate the space-time variations of ice and the underlying mechanisms in Lake Nam Co, the third largest lake over Tibetan Plateau. The numerical model reasonably reproduces the seasonal evolution of ice coverage from satellite remote sensing and ice thickness from in situ observations. Model results reveal that the eastward drift of thin ice throughout the ice-covered phase and eastward water heat transport during the ice melting phase, which are related to the prevailing westerly, are key factors controlling the spatial variation of lake ice. The ice area, volume, duration, ice-on date and ice-off date all show large interannual variability, which can be mostly attributed to the "cumulative effects" of surface air temperature over different preceding months.

Key Points:

- Analysis of hydrodynamic-ice simulations gains insights on spatiotemporal variations in ice cover and underlying mechanisms in Lake Nam Co
- Eastward drift of thin ice and water heat transport (related to westerly) are main factors determining the spatial variation of lake ice
- Significant interannual variations of lake ice volume and phenology are closely related to "cumulative effects" of surface air temperature

Supporting Information:

Supporting Information may be found in the online version of this article.

Correspondence to:

A. Huang,
anhuang@nju.edu.cn

Citation:

Wu, Y., Huang, A., Lu, Y., Fujisaki-Manome, A., Zhang, Z., Dai, X., & Wang, Y. (2023). Application of a three-dimensional coupled hydrodynamic-ice model to assess spatiotemporal variations in ice cover and underlying mechanisms in Lake Nam Co, Tibetan Plateau, 2007–2017. *Journal of Geophysical Research: Atmospheres*, *128*, e2023JD038844. https://doi.org/10.1029/2023JD038844

Received 7 MAR 2023
Accepted 23 NOV 2023

Author Contributions:

Conceptualization: Anning Huang
Data curation: Yang Wu, Ayumi Fujisaki-Manome, Zhiqi Zhang, Xianglin Dai, Yu Wang
Formal analysis: Yang Wu, Youyu Lu
Investigation: Yang Wu, Anning Huang, Youyu Lu
Methodology: Yang Wu, Anning Huang
Resources: Ayumi Fujisaki-Manome
Software: Yang Wu, Ayumi Fujisaki-Manome, Yu Wang
Supervision: Yang Wu, Anning Huang
Validation: Yang Wu, Youyu Lu
Visualization: Yang Wu, Anning Huang, Youyu Lu, Zhiqi Zhang

1. Introduction

The Tibetan Plateau (TP) has widely and densely distributed alpine lake systems (Zhang, Chen, et al., 2020), which greatly influence the regional weather and climate mainly via altering the turbulent flux exchanges at the lake-air interface (Su et al., 2020; Wu et al., 2019, 2020). Due to the harsh winter condition over TP, these alpine lakes are usually ice-covered for 4–5 months in a year (Kirillin et al., 2017). The formation and ablation of ice play a vital role in determining the lake-air interactions and thus the thermo-hydrodynamics (Bai et al., 2020; Jansen et al., 2021). Ice cover inhibits the moisture, heat, and momentum fluxes between water and air, leading to delayed lake warming, weakened circulations, as well as potential shifts in a wide range of biogeochemical

Writing – original draft: Yang Wu
Writing – review & editing: Yang Wu, Anning Huang, Youyu Lu, Ayumi Fujisaki-Manome, Xianglin Dai

processes (Fujisaki et al., 2012, 2013; Woolway & Merchant, 2019; Woolway et al., 2021). In addition, lake ice has been identified as an essential climate factor in understanding and predicting the evolution of hydroclimate and environment over TP (Zhang, Yao, et al., 2020), one of the most sensitive regions to global climate change (Yao et al., 2012, 2019). Addressing the spatiotemporal variations of ice cover and the underlying mechanisms is crucial for advancing the knowledge of the TP ice-lake systems due to the thermo-hydrodynamic and ecological relevance.

Recognizing the importance, various research projects have promoted the establishment of meteorological and hydrological stations in several large lakes over TP, which effectively enriched the continuous monitoring of water temperature profiles, turbulent fluxes, ice/snow process and under-ice thermodynamics (Biermann et al., 2014; Li et al., 2015; Qu et al., 2012; Wang et al., 2019, 2020). Field measurements over Lake Ngoring, the largest freshwater lake over TP, showed that the ice surface albedo is generally less than 0.3, lower than that observed in temperate plain lakes or estimated using common ice-albedo parameterizations (Li et al., 2018). This was attributed to the strong blowing snow effect and less snow cover over TP lakes. Similar phenomenon of reduced ice albedo was reported for Lake Aksai Chin, Lake Zhari Namco, Lake Qinghai, Lake Jingyu and Lake Nam Co (LNC; Lang et al., 2018). During the ice melting phase, the rapid under-ice water warming and stratification development were reported to widely occur in TP lakes (Huang, Zhang, et al., 2019, Huang, Lazhu, et al., 2019; Kirillin et al., 2021; Lazhu et al., 2020). This was related to the easy penetration of solar radiation through the highly transparent ice, as noted in previous studies (e.g., Birge, 1910; Woodcock, 1965). In addition to in situ observations, active/passive microwave and multispectral remote sensing technologies have been utilized to monitor the lake ice over TP since the 1980s, with the main focus on the interannual variations of ice phenology from the lake-averaged perspective (Cai et al., 2019; Kropacek et al., 2013; Yao et al., 2016). An important consensus is that most TP lakes, that is, Lake Qinghai (Cai et al., 2017; Qi et al., 2019, 2020) and LNC (Gou et al., 2017; Ke et al., 2013), are undergoing substantial alternations in ice phenology, featured by delayed freezing, shortened ice duration, and earlier thawing in response to regional air warming. However, limited by the inadequate space-time resolutions and cloud contamination of satellite-derived images (Guo et al., 2018), analyses with the images only are inadequate to address the space-time variations of ice cover and the underlying mechanisms.

Three-dimensional (3-D) coupled hydrodynamic-ice models serve as effective tools to study the large lake-ice systems, for example, the Laurentian Great Lakes, where the ice cover features strong spatial variability and large interannual variability in its seasonal cycles (Lin et al., 2022; Wang et al., 2012). Wang et al. (2010) developed a Great Lakes Ice-circulation Model (GLIM) and carried out a hindcast simulation with a 2-km horizontal resolution for the 2003–2004 ice season of Lake Erie. The model results were analyzed to study the ice variation, as well as its impacts on variations of the thermal structure, circulation, and water level. Ongoing ice modeling studies reveal that the strong interannual variability of ice in the Laurentian Great Lakes is sensitive to the air temperature variability under the modulation of climate teleconnection patterns (Fujisaki et al., 2013). During the years with lower ice coverage, the lake circulation and the water level including waves and seiches are more energetic due to the decreased strength of ice-water stress and wave-ice interactions (Bai et al., 2020; Fujisaki et al., 2012). With the long-term decline in ice cover for all of the Laurentian Great Lakes (Austin & Colman, 2007; Bai et al., 2012), considerable changes in lake physical structure (e.g., thermal structure and circulation) and ecosystems are expected to occur more frequently. White et al. (2012) applied the Regional Oceanic Modeling System (ROMS) that includes ice and biogeochemical components to Lake Superior. The analysis of the simulation results revealed the correspondence among the increasing annual air temperature, decreasing winter ice-cover, and increasing annual water temperature and gross primary productivity. Furthermore, the hydrodynamic-ice model has been coupled to an atmosphere model to account for lake-air interactions to improve the regional climate simulations over Laurentian Great Lakes (Fujisaki et al., 2020; Sun et al., 2020; Xue et al., 2017).

Encouraged by the lake-ice modeling studies on Laurentian Great Lakes, a hydrodynamic-ice model is adopted in this study to carry out multi-year simulations of lake thermo-hydrodynamics and ice in LNC, the third largest lake located over TP. This study extends the previous work of Wu et al. (2021) that is based on the 3-D hydrodynamic Princeton Ocean Model (POM) without including the ice component. Based on the simulation for the ice-free phase within 1 year, Wu et al. (2021) revealed the effect of the lateral water heat transport in determining the spatial variability of lake thermal structure and the important role of the prevailing southwesterly wind in inducing the lake circulation in LNC. However, for this large lake-ice system with 5 months of ice coverage, three key questions remain to be addressed: (a) what are the spatiotemporal variations and driving mechanisms of ice? (b) how does the presence of ice affect the lake thermo-hydrodynamics? And, (c) is there interannual variability

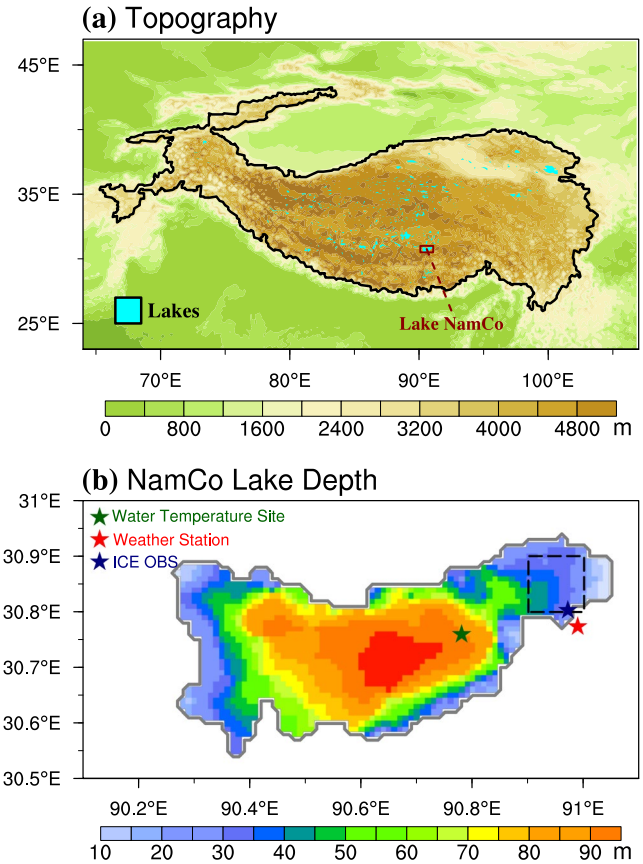

Figure 1. (a) Spatial distribution of land topography and lakes (lightblue colored areas) over TP. (b) Bathymetry of LNC with 1 km horizontal resolution. The darkgreen and red stars represent the LNC mooring site and the weather station, respectively. The navy-blue star denotes the mean location of the ice thickness observation transect. The black rectangle box outlines the eastern LNC (30.8–30.9°N, 90.9–91.0°E) used for analysis shown in Figure 5.

of the lake circulation during the ice-free phase and what are the influencing factors? To address the above questions, we apply a three-dimensional lake-ice coupled model, for the first time, for multi-year simulations in LNC. In this paper, we focus on verifying the model performance and analyzing the spatiotemporal variations of ice cover and the underlying mechanisms. A companion paper will analyze the interannual variations of lake circulation and thermal structure.

In the remaining parts of this paper, after introducing the data and model setup (Section 2), model performance will be extensively verified with available in situ and satellite-derived observations (Section 3); model analyses will be carried out to quantify the space-time variations of ice concentration, thickness, drift, and phenology, and to explore the underlying mechanisms of these variations (Section 4); the advantages of 3-D versus one-dimensional (1-D) models, including the ice dynamics for ice simulation and the coupling of ice for lake hydrodynamic simulation, as well the model limitations of this study, will be discussed (Section 5); and finally, the main findings of this study and recommendation for future studies will be provided (Section 6).

2. Data and Model Setup

2.1. Study Area

According to the spatial distribution maps of lakes over TP (Figure 1; Zhang et al., 2019; available at https://data.tpdc.ac.cn/en/), LNC (30.50°N–30.92°N, 90.27°E–91.05°E; approximately 4,730 m above sea level) is the third largest lake. It is located at the northeastern foot of the elevated Nyainqentanglha Mountains (~6,000 m altitude) over central TP. LNC has a surface area exceeding 2,000 km^2 and a maximal depth of ~99 m (Wang et al., 2009, 2019). LNC is a typical dimictic lake, with a thermally stratified phase during June-October and an ice-covered phase during January–April. The Nam Co basin is climatically influenced by the summer southwesterly and winter westerly wind (Wang et al., 2020; You et al., 2007).

2.2. Data Sets and Methods

The in situ and satellite-derived data sets used to verify the model forcing and simulation results are summarized in Table 1, with the details listed as follows:

1. Daily meteorological records from the integrated observation and research station of multiple spheres in LNC (30.77°N, 90.99°E, red star in Figure 1b). Available surface meteorological parameters include near-surface

Table 1
Descriptions of the Data Sets Used in This Study

Data type	Description	Location or spatial resolution	Temporal resolution	Length
In situ	Meteorological records	(30.77°N, 90.99°E)	Daily	2005–2016
	Water temperature profile	(30.76°N, 90.78°E)	Daily	2011–2014
	Ice thickness transect	Centered around (30.80°N, 90.97°E)	~biweekly	2007–2011
Satellite remote sensing	Lake surface temperature based on MOD11A1	Lake-mean	Daily	2000–2017
	Surface reflectivity from MOD09GQ	250 m	Daily	2000–2023
Meteorological reanalysis	CMFD	0.1°	3-hourly	1979–2018
	ERA5_Land	0.1°	Hourly	1950–2023

radiation, relative humidity, air temperature, pressure, and wind speed during 2005–2016 (https://data.tpdc.ac.cn/en/, Wu, 2018).

2. Daily water temperature profiles from a mooring site located in the eastern part of the central basin of LNC (30.76°N, 90.78°E, darkgreen star in Figure 1b). Available data were sampled at depths of 3, 6, 16, 21, 31, 36, 56, 66, and 83 m during 2011–2014 (https://data.tpdc.ac.cn/en/, Wang, 2020).
3. Ice thickness observations along a transect located near the southeastern shore of LNC. During 2007–2011, the ice thickness measurements began after the lake was completely frozen during early January, and ended when the ice started to break up in early April, with sampling intervals of ∼2 weeks. At each sampling date, the sampling usually started from near the southeastern shore and extended 2 km northeastward, with the transect located around (30.80°N, 90.97°E) (navy-blue star in Figure 1b). The ice thickness observations did not account for the ice composition and the snow depth on ice. More details are described in Qu et al. (2012).
4. Daily lake-wide mean surface temperature (LST) over LNC obtained from an integrated data set for 160 lakes across the TP. Note that the LST is the average of water surface temperature and ice surface temperature, weighted with the ice concentration. The data set includes daytime, nighttime, and daily mean LST during 2000–2017 retrieved from MOD11A1 (https://doi.org/10.5281/zenodo.5111400, Guo et al., 2021). The data set has been well verified with other satellite-based LST products and is valuable for investigating the long-term LST variability across TP.
5. The estimated daily surface reflectivity for the red (620–670 nm, band 1) and near-infrared (841–876 nm, band 2) bands from the MOD09GQ version 6 product (Vermote & Wolfe, 2015). The product is in the sinusoidal projection and has a resolution of 250 m. As the red/near-infrared reflectance of ice is far higher than that of water, the lake ice is detected by compositing the nearly cloud-free surface reflectivity images with the order of band 1-2-1 on the Google Earth Engine platform (Kumar & Mutanga, 2019).

Finally, the China Meteorological Forcing Data set (CMFD), which was documented to be well-suited for land and hydrological modeling over China, is utilized as the meteorological forcings to drive the three-dimensional lake-ice coupled model. CMFD includes the surface downward shortwave and longwave radiation, surface air pressure, 2-m air temperature and relative humidity, and 10-m wind speed during 1979–2018 at 3-hourly intervals and with a horizontal resolution of 0.1° (https://data.tpdc.ac.cn/en/, He et al., 2020). Figure 2a–2e show that CMFD is consistent with the time evolution and magnitudes of the in situ observations of surface downward shortwave and longwave radiation, 2-m air temperature and relative humidity, whereas it underestimates the 10-m wind speed. Because CMFD is a fusion product assimilating a vast amount of land-based observations, the underestimation of over-lake wind speed is likely at due to neglecting the wind acceleration over the lake due to the reduced surface roughness compared with on land. Thus, the over-lake wind speed (Y) is obtained by adjusting the CMFD wind speed (X) according to $Y = 1.17X + 1.62$ as suggested by Hsu (1988), whose applicability was well verified among 244 globally distributed large lakes by Layden et al. (2016), and among 94 large lakes in China by Huang, Wang, et al. (2021). From Figure 2e, the corrected time series match well with the in situ observations, with the mean bias (BIAS) and root mean square error (RMSE) reduced to 0.20 $m{\cdot}s^{-1}$ and 1.20 $m{\cdot}s^{-1}$, from the corresponding values of -1.89 $m{\cdot}s^{-1}$ and 2.23 $m{\cdot}s^{-1}$ prior to the adjustment. The wind direction, which is not available in CMFD, is obtained by interpolating the that from the ERA5_Land reanalysis (https://cds.climate.copernicus.eu; Muñoz-Sabater, 2019) onto the CMFD grids. From Figure 2f, the ERA5_Land wind direction is consistent with the in situ observed prevailing southwesterly over LNC. Figure 3 presents the monthly wind field averaged over 2007–2017, which depicts the prevailing of southwesterly over LNC and the larger wind speed during September-February than during March-August.

After obtaining the model simulation results, the relative contributions of surface wind and current to the ice drift is analyzed using a multiple linear regression analysis (Chatterjee & Hadi, 1986) in the following form:

$$\overrightarrow{V}_i = R_w e^{i\theta_w}\overrightarrow{V}_w + R_c e^{i\theta_c}\overrightarrow{V}_c + R \quad (1)$$

where $\overrightarrow{V}_i$, $\overrightarrow{V}_w$, and $\overrightarrow{V}_c$ denote the horizontal ice drift, surface wind and current velocity, respectively, all in complex form (in $m{\cdot}s^{-1}$); R_w (R_c) is the regression coefficient for wind (current) magnitude, θ_w (θ_c) is the regressed ice drift angle to the right of wind (current); and R is the residual term. The above ice-wind-current relationship is suitable for free ice drift with the assumption that the internal ice stress is negligible, and has been widely used in previous analyses of ice drift in the Bohai Sea (Li et al., 2020; Wu et al., 2005; Yan et al., 2019).

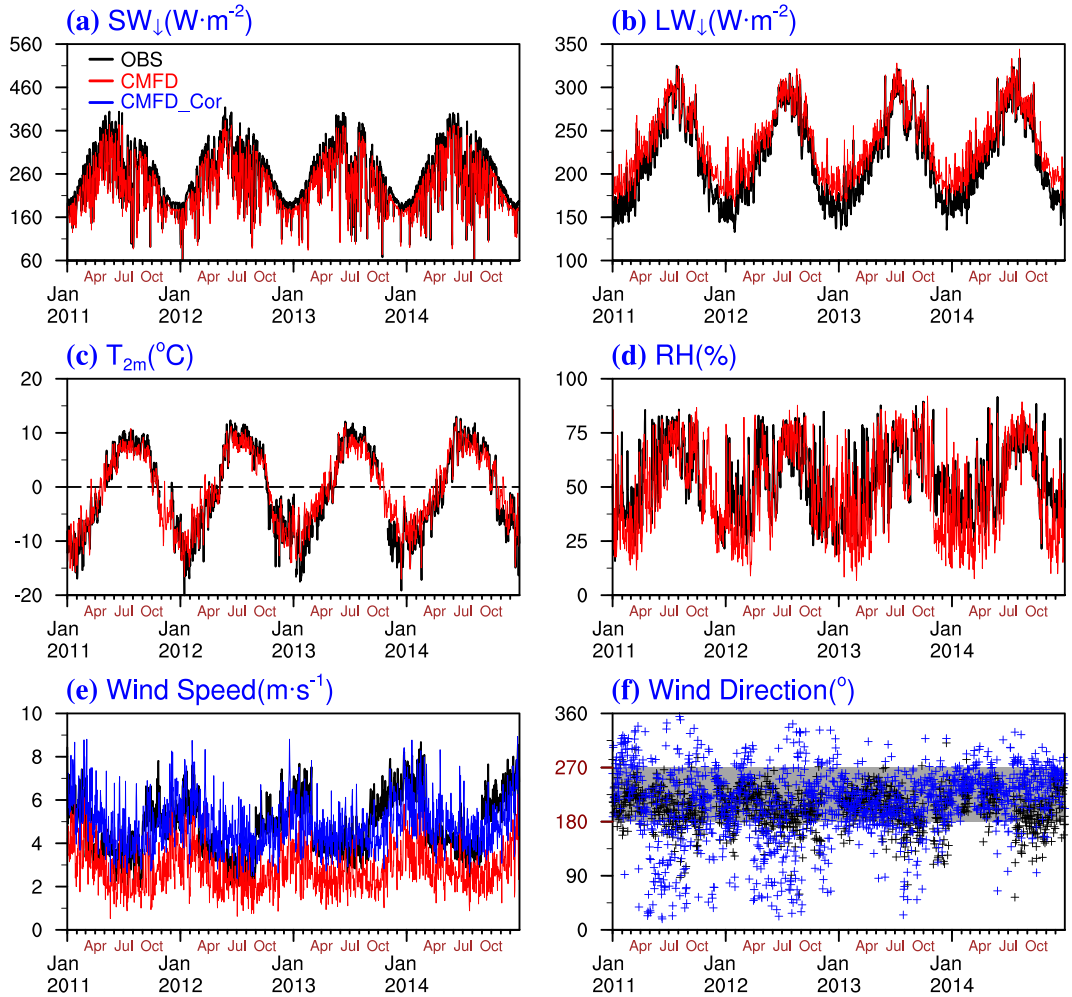

Figure 2. The daily surface (a) downward shortwave radiation, (b) downward longwave radiation, (c) air temperature, (d) relative humidity, (e) wind speed, and (f) wind direction during 2011–2014 from in situ observations (black) and CMFD data sets (red in a-e). In (e), the blue line denotes the adjusted CMFD wind speed. In (f), the blue markers denote the wind direction from the ERA5_Land reanalysis. The wind direction is calculated in 0–360° clockwise from due north, and the gray shading range of 180–270° in (f) corresponds to the southwesterly wind. Note the reference height is 2 m for the CMFD air temperature and relative humidity, and 10 m for the CMFD wind speed and ERA5_Land wind direction. No height correction is applied to the in situ observations from the meteorological station.

The effective ice thickness at a grid point i is defined as AH_i, where A_i is ice concentration and H_i (in m) is ice thickness. The ice volume is defined as the product of effective ice thickness and grid area. The changes of effective ice thickness ($\Delta\mathrm{AH}_i$) over each ice season can be expressed as:

$$\Delta\mathrm{AH}_i = \Delta\mathrm{AH}_{\mathrm{freeze}} + \Delta\mathrm{AH}_{\mathrm{melt}} + \Delta\mathrm{AH}_{\mathrm{adv}} \quad (2)$$

where $\Delta\mathrm{AH}_{\mathrm{freeze}}$, $\Delta\mathrm{AH}_{\mathrm{melt}}$, and $\Delta\mathrm{AH}_{\mathrm{adv}}$ are the changes of AH_i due to freezing, melting, and advection, respectively. For the four terms in Equation 2, positive (negative) value means the ice accumulation (loss). $\Delta\mathrm{AH}_{\mathrm{freeze}}$ ($\Delta\mathrm{AH}_{\mathrm{melt}}$) at each time step of ice thermodynamics is determined as $-W_{\mathrm{iw}}/\rho_i$ if W_{iw} is negative (positive), where W_{iw} is the downward freshwater flux due to ice freezing/melting (in $\mathrm{kg\cdot m^{-2}\cdot s^{-1}}$), and $\rho_i = 910\ \mathrm{kg\cdot m^{-3}}$ is the ice density. As the ice in LNC is completely "reset" each year, $\Delta\mathrm{AH}_{\mathrm{adv}}$ can be calculated according to $-(\Delta\mathrm{AH}_{\mathrm{freeze}} + \Delta\mathrm{AH}_{\mathrm{melt}})$.

2.3. Lake-Ice Coupled Model

The ice-coupled Princeton Ocean Model (ICEPOM) is used in this study. ICEPOM couples the 3-D Princeton Ocean Model (POM) and a two-dimensional thermo-hydrodynamic ice model, and has been successfully

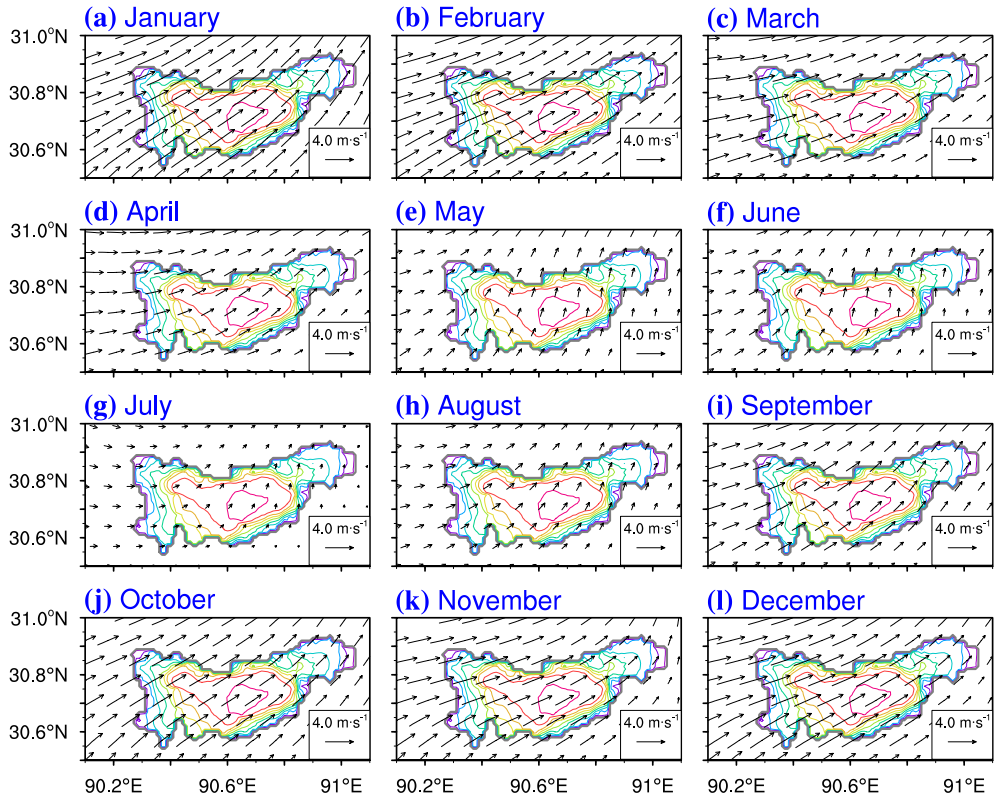

Figure 3. The monthly mean wind fields at 10 m averaged over 2007–2017 from the calibrated CMFD data sets. The contour lines denote lake depths in 10 m intervals.

applied to the Arctic Ocean and Laurentian Great Lakes (De Silva et al., 2015; Fujisaki et al., 2012, 2013; Wang et al., 2005). POM solves nonlinear governing equations of lake water motions, temperature and salinity including the hydrostatic and Boussinesq approximations, using the finite difference method (Blumberg & Mellor, 1987; http://www.ccpo.odu.edu/POMWEB/POM08_WAD/). The settings of POM follow Wu et al. (2021), including the horizontal grids with 1-km spatial resolution (Figure 1b), and 31 terrain-following sigma levels with finer resolution near the surface/bottom. In this application, POM uses turbulence closure scheme proposed by Mellor and Yamada (1982), horizontal mixing scheme proposed by Smagorinsky (1963), equation of state of Mellor (1991), adiabatic closed lateral/bottom boundaries, quadratic bottom drag coefficient, and infrared/optical radiation partitioning and the related vertical extinction coefficients. The only difference with the POM setup of Wu et al. (2021) is that the algorithms of surface turbulent heat flux (with constant bulk transfer coefficients) and wind stress are replaced with the version 3.0 algorithm of the Coupled Ocean-Atmosphere Response Experiment (Fairall et al., 1996, 2003), following Charusombat et al. (2018).

The ice dynamic component employs a two-dimensional dynamic model based on the elastic-viscous-plastic rheology (Hibler, 1979, 1980; Hunke & Dukowicz, 1997), with one category of ice thickness. The ice motion is solved by the momentum equation:

$$m\frac{d\vec{V}_i}{dt} = -mf\vec{k}\times\vec{V}_i - \mathrm{mg}\nabla\mathrm{ssh} + \vec{\tau}_{\mathrm{ai}} + \vec{\tau}_{\mathrm{wi}} + \vec{F}_i \tag{3}$$

Where $m = \rho_i A_i H_i$ is ice mass of unit area (in kg·m^{-2}), f is the Coriolis parameter (in s^{-1}), $g = 9.80616$ m·s^{-2} is the gravitational acceleration, ∇ssh is the gradient of water surface elevation, and $\vec{F}_i$ is the internal stress (in N·m^{-2}). The air-ice and water-ice stress, $\vec{\tau}_{\mathrm{ai}}$ and $\vec{\tau}_{\mathrm{wi}}$, are determined by the bulk formulae:

$$\vec{\tau}_{\mathrm{ai}} = \rho_a C d_{\mathrm{ai}} \left|\vec{V}_a - \vec{V}_i\right| \left(\vec{V}_a - \vec{V}_i\right) \tag{4}$$

$$\vec{\tau}_{\mathrm{wi}} = \rho_w C d_{\mathrm{wi}} \left|\overrightarrow{V}_w - \overrightarrow{V}_i\right| \left(\overrightarrow{V}_w - \overrightarrow{V}_i\right) \tag{5}$$

where ρ_a and ρ_w are densities of the moist air and water (in kg·m^{-3}), $\overrightarrow{V}_a$ and $\overrightarrow{V}_w$ are the horizontal velocities of air and water (in m·s^{-1}), $\mathrm{Cd_{ai}} = 0.003$ and $\mathrm{Cd_{wi}} = 0.006$ are the drag coefficients at the air-ice and water-ice interfaces. $\mathrm{Cd_{ai}}$ is reduced to 0.001 when the ice thickness is less than 0.01 m.

The ice component employs a 0-layer thermodynamic model (Parkinson & Washington, 1979; Semtner, 1976) without considering the snow accumulation. New ice forms when the surface water temperature drops below the freezing point (T_{frz}) which varies with water salinity (Millero, 1978) and equals to −0.09°C with a salinity of 1.7 g L^{-1} for LNC. The ice surface temperature (T_{i_sur}) is determined by the surface energy balance:

$$(1 - I_0)(1 - \alpha_i)\mathrm{SW}_{\downarrow} + \varepsilon_i \mathrm{LW}_{\downarrow} - \varepsilon_i \sigma T_i^4 - \mathrm{SH_{i,\uparrow}} - \mathrm{LH_{i,\uparrow}} + G_{i,\uparrow} = 0 \tag{6}$$

where $\mathrm{SW}_{\downarrow}$ is the downward solar radiation (in W·m^{-2}), $I_0 = 40\%$ is the fraction of net $\mathrm{SW}_{\downarrow}$ penetrating the snow-free ice surface, $\mathrm{LW}_{\downarrow}$ is the downward longwave radiation (in W·m^{-2}), $\varepsilon_i = 0.97$ is the longwave emissivity of ice, and $\sigma = 5.67 \times 10^{-8}$ W·m^{-2} K^{-4} is the Stefan-Boltzmann constant. The other terms are defined below. First, the surface ice albedo α_i is not set as a default constant value of 0.6, but is calculated with a temperature-dependent scheme (Subin et al., 2012):

$$\alpha_i = \alpha_{i\max} - (\alpha_{i\max} - \alpha_{i\min}) e^{-95.6(T_{\mathrm{frz}} - T_{i\_\mathrm{sur}})/T_{\mathrm{frz}}} \tag{7}$$

where $\alpha_{i\max}$ and $\alpha_{i\min}$, the maximum and minimum values of α_i, are assumed to be 0.5 and 0.1 for snow ice and bare melting ice according to the MODIS-retrieved observations over LNC (Lang et al., 2018). As reviewed in the introduction section, the values of α_i are generally less than 0.3 based on field observations over the largest freshwater lake (Lake Ngoring; Li et al., 2018). The upward sensible ($\mathrm{SH_{i,\uparrow}}$) and latent ($\mathrm{LH_{i,\uparrow}}$) heat fluxes across the air-ice interface are calculated according to:

$$\mathrm{SH}_{i,\uparrow} = \rho_a C_{pa} C_{\mathrm{shi}} (T_{i\_\mathrm{sur}} - T_a) \left|\overrightarrow{V}_a\right| \tag{8}$$

$$\mathrm{LH}_{i,\uparrow} = \lambda_{\mathrm{vi}} \rho_a C_{\mathrm{lhi}} (q_i - q_a) \left|\overrightarrow{V}_a\right| \tag{9}$$

where $C_{\mathrm{pa}} = 1005$ J·kg^{-1} K^{-1} is the specific heat of air, $C_{\mathrm{shi}} = 0.00175$ ($C_{\mathrm{lhi}} = 0.00175$) is the bulk constant coefficient of sensible (latent) heat, T_a is the surface air temperature (in °C), $\lambda_{\mathrm{vi}} = 2.8 \times 10^6$ J·kg^{-1} is the latent heat of sublimation, q_i and q_a are the saturated specific humidity of surface ice and specific humidity of air at 10 m (in kg^{-1} kg^{-1}). Finally, the upward internal conductive heat flux through ice ($G_{i,\uparrow}$) is calculated according to:

$$G_{i,\uparrow} = \frac{k_i}{H_i}(T_{i\_\mathrm{bot}} - T_{i\_\mathrm{sur}}) \tag{10}$$

where $k_i = 2.04$ W·m^{-1} K^{-1} is the thermal conductivity of ice, and T_{i_bot} is the ice bottom temperature that is assumed to equal T_{frz}. In the case that T_{i_sur} predicted by Equation 6 exceeds T_{frz}, T_{i_sur} is set to T_{frz}, then the surface energy budget is recalculated with $T_{i\_\mathrm{sur}} = T_{\mathrm{frz}}$ and the resulting excess energy is used to melt the surface ice. At the bottom of ice, the rate of ablation or accretion ($\frac{dH_i}{dt}$) is determined by the heat imbalance between $G_{i\uparrow}$ and the upward oceanic heat flux ($fb_{\uparrow}$), as formulated by:

$$\frac{dH_i}{dt} = (fb_{\uparrow} - G_{i,\uparrow})/Q_i \tag{11}$$

$$fb_{\uparrow} = \rho_w C_{\mathrm{pw}} C_h u^* (T_{i\_\mathrm{bot}} - T_{w\_\mathrm{sur}}) \tag{12}$$

where $Q_i = 3.3 \times 10^5$ J·kg^{-1} is the heat of ice fusion, $C_{\mathrm{pw}} = 4186$ J·kg^{-1} K^{-1} is the specific heat of water, $C_h = 0.005$ is the ice-water heat transfer coefficient (McPhee et al., 2008), u^* is the friction velocity (in m·s^{-1}) at the ice-water interface, and T_{w_sur} is the water surface temperature (in °C). In addition to the surface and basal ice variations, a parameterization for lateral freezing and thawing caused by the energy flux of the open water is also implemented (Ohshima & Nihashi, 2005). More Details of the above parameterizations can be found in Parkinson and Washington (1979).

ICEPOM is initialized on 20 May 1999 for a continuous run until 31 December 2017. The model is initialized with zero currents, zero ice cover, a salinity of 1.7 g L^{-1}, and a uniform temperature of 2.52°C which is the LST from Guo et al. (2021) on 20 May 1999. The time steps for the hydrodynamic model are set to 1 s for the external mode (depth-integrated flow and water level) and 60 s for the internal mode (depth-varying flow, temperature, and salinity). The time steps for ice component are set to 20 s for the ice dynamics and 60 s for the ice thermodynamics. The model is run on a 48-core parallel computing cluster, and it takes ∼2 min to complete 1-day simulation. Considering the available in situ ice thickness records starting from 2007, we take 1999–2006 as a sufficiently long spin up phase and evaluate and analyze the model results from 2007 onward.

3. Model Evaluation

Following Huang, Lazhu, et al. (2019), three statistical parameters, that is, the Pearson temporal correlation (TC), the mean bias (BIAS), and root mean square error (RMSE) are used for model evaluation against the in situ measured ice thickness and water temperature profile, and satellite retrieved LST. We define winter as from December to the following February, spring as March to May, summer as June to August, and autumn as September to November. Simulated LST is calculated as the sum of the water surface temperature and ice surface temperature weighted by $(1-A_i)$ and A_i, respectively.

3.1. Seasonal Variations of Lake Ice Cover and Thickness

Figure 4 shows the ice extent from the MOD09GQ satellite reflectivity images and the effective ice thickness and drift velocities from model simulations in 5 days during January–May, 2014. According to the satellite observations, the lake ice first forms over the eastern basin in early January. From February to March, the lake ice expands from the eastern to the western LNC to nearly covers the entire lake, with higher ice concentration in the eastern LNC. On April 10, ice coverage is reduced with large areas of open water in the western LNC. On May 5, ice almost disappears except for a small amount in the eastern LNC. Such seasonal evolution of freezing/melting process, that is, that LNC freezes up from east to west and ice breaks up from west to east, was reported by Qu et al. (2012) and Gou et al. (2017) based on analyses of MOD09GQ images during 2006–2011 and during 2000–2015. The seasonal variation of ice extent from ICEPOM reasonably agrees with that based on the MOD09GQ satellite images, despite that ICEPOM produces less ice coverage in the western LNC during March and April. In addition, the model replicates widespread eastward drift of thin ice (<5 cm) during January-March, consistent with the direction of the prevailing westerly surface wind.

Figure 5 compares the measured ice thickness averaged over the drilling transect and the simulated effective ice thickness averaged over the eastern LNC (30.8–30.9°N, 90.9–91.0°E) at each sampling date during 2007–2011. A review of the ice drilling data during 2007–2011 reveals that the ice thickness increases during January and February, peaks at ∼60 cm in March, and then decreases since April. ICEPOM reasonably reproduces the seasonal evolution of ice thickness, but shows an overall overestimation with BIAS ranging from 2.1 to 16.6 cm and a mean value of 8.2 cm. The model overestimates the ice thickness by the maximum values of ∼30 cm during 2010 and 2011, indicating the need to improve the model in replicating the ice growth. Similar ice thickness overestimation with a BIAS exceeding 25 cm was reported in a previous application of ICEPOM in Lake Erie (Fujisaki et al., 2013), and was attributed to the lack of sub-grid scale ice thickness distribution to account for processes such as the breaking and overturning of large ice floes. In the eastern LNC, the redistribution of ice thickness by the continuity equation may result in excessively wind-driven mechanical convergence of ice. The issue of ice thickness overestimation may be remedied using alternative mechanical deformation models (e.g., Thorndike et al., 1975). Figure 5 also shows the ICEPOM simulated daily lake-wide averaged ice thickness increases from mid-December to March, peaks around mid-March, and decreases from April to early June.

3.2. Lake Surface Temperature

Figure 6 compares the daily time series of the lake-wide averaged LST from MODIS, and the water temperature at 3 m depth ($TLake_{3m}$) from in situ observations, with the simulation results of ICEPOM. Figure 7 shows the annual and seasonal lake-wide averaged LST from MODIS observation and ICEPOM simulation during 2007–2017, as well as the multi-year means of monthly LST.

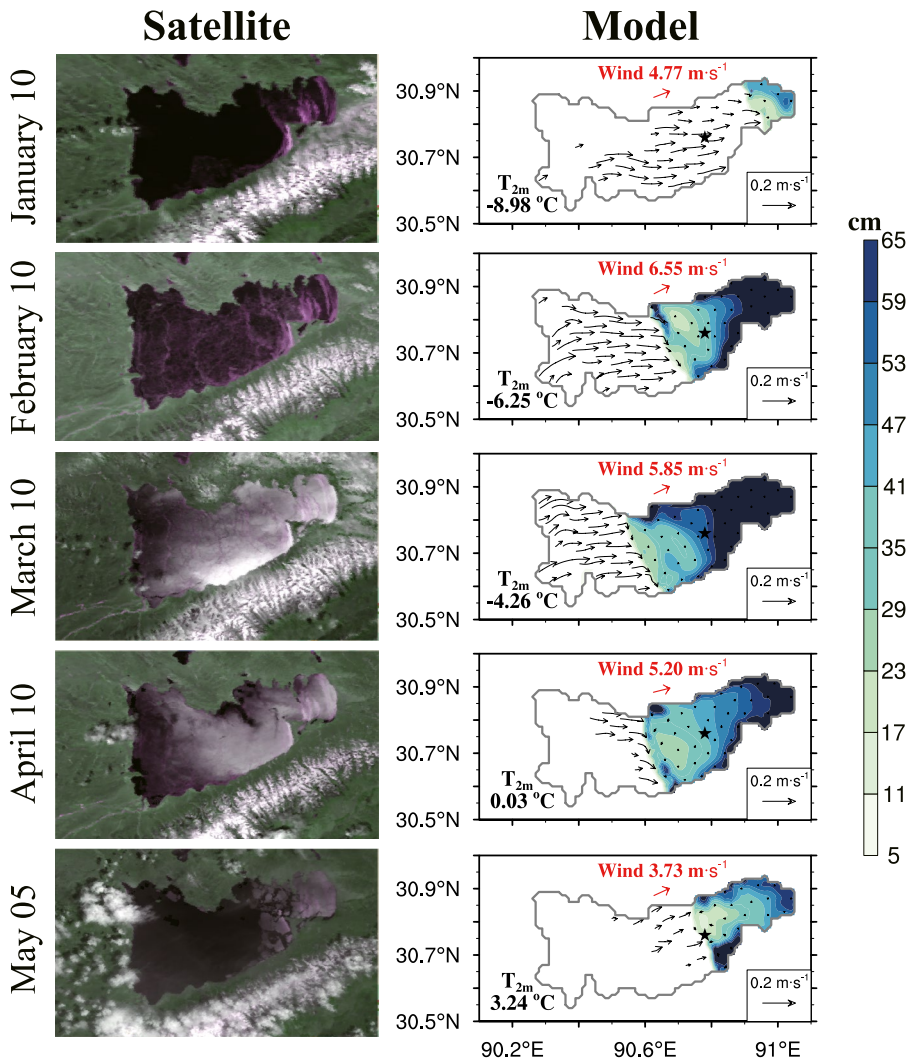

Figure 4. The freezing/melting processes of LNC in 2014. Left column: the MOD09GQ satellite images with the false color composite band 1-2-1, within LNC ice being denoted by the purple or white color, and open water by the black color. Right column: model simulations with color shading depicting the effective ice thickness, vectors representing the ice drift, text in black denoting the lake-wide averaged near-surface air temperature, text and arrows in red denoting the lake-wide averaged surface wind, and the black stars marking the mooring site.

From Figure 6a, LNC is a typical seasonally ice-covered dimictic lake: (a) The lake is ice-covered for 4–5 months during winter and spring, with the MODIS observed lake-wide averaged LST of −1.52°C and −1.87°C, respectively (Figure 7). (b) The lake is stratified for 4–5 months during summer and autumn, with the MODIS observed lake-wide averaged LST of 7.85 and 7.65°C, respectively (Figure 7). ICEPOM reasonably reproduces the observed seasonal evolution of LST, with a TC of 0.94, but exhibits a positive BIAS of 1.11°C during 2007–2017 (Figure 6a). Considering that the satellite-retrieved LST over TP is usually lower than the in situ observed values by 0.8–1.9°C due to the cool skin effects (Hook et al., 2003; Ke & Song, 2014), it is highly likely that the BIAS is very small with reference to the actual LST values during the warm season. During winter-spring, the model may produce less ice and overestimate LST because the current ICEPOM does not take into account the snow cover process and the snow ice albedo is set to 0.5, lower than 0.6 that can be reached during the presence of extensive snow cover in LNC (Lang et al., 2018). Exact determination of the accuracy of the modeled LST requires further ground-truthing of the satellite data. ICEPOM well reproduces the observed $TLake_{3m}$ variability, yielding a TC of 0.98, a BIAS of −0.57°C, and a RMSE of 0.95°C (Figure 6b).

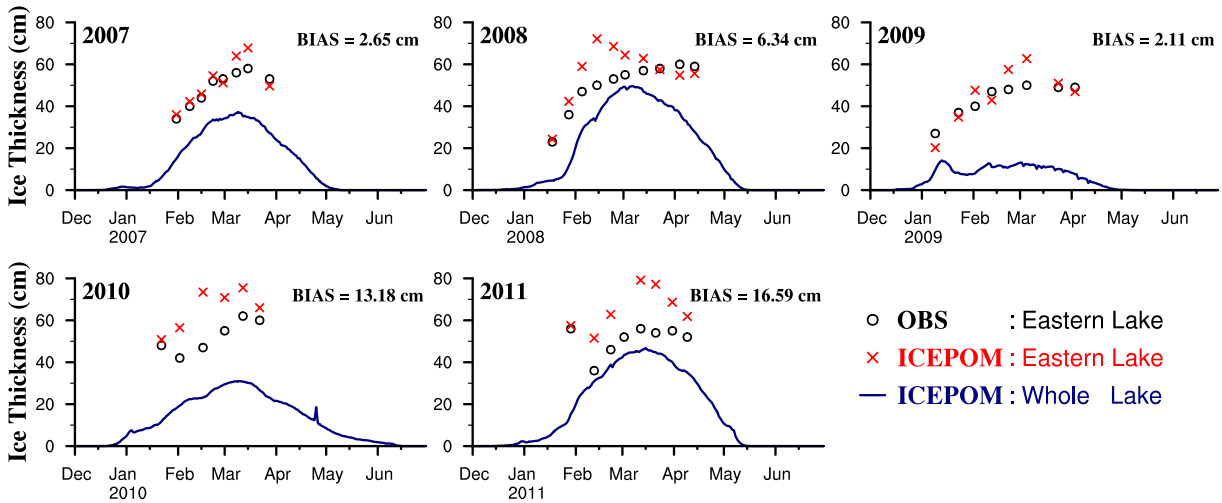

Figure 5. Mean observed ice thickness along the in situ drilling transect (black circles) and the ICEPOM simulated effective ice thickness averaged over the eastern LNC (red crosses) at each sampling date during 2007–2011. The blue lines denote the daily time series of lake-wide averaged effective ice thickness from ICEPOM simulations.

The magnitude and interannual variations of LST from ICEPOM agree well with that from MODIS (Figures 7a–7e), with the TC (RMSE) of 0.66–0.84 (0.69–1.69°C). In winter and spring, LST has larger spatial variations across the lake than in summer and autumn, evident from the shaded bands for the ICEPOM results shown in Figures 7a–7e. The larger LST spatial heterogeneity during winter and spring corresponds to the temperature difference between ice-covered and ice-free lake surfaces. The lake-wide averaged LST also shows larger interannual variability in winter and spring, according to both MODIS and ICEPOM (Figure 7). From Figure 7f, ICEPOM reasonably reproduces the climatology of monthly LST, with a TC of 0.99 and a RMSE of 1.20°C. The lake-wide averaged LST shows larger interannual variability during February-March, with standard deviations of 2.74–1.51 (1.92–1.43) °C according to MODIS (ICEPOM).

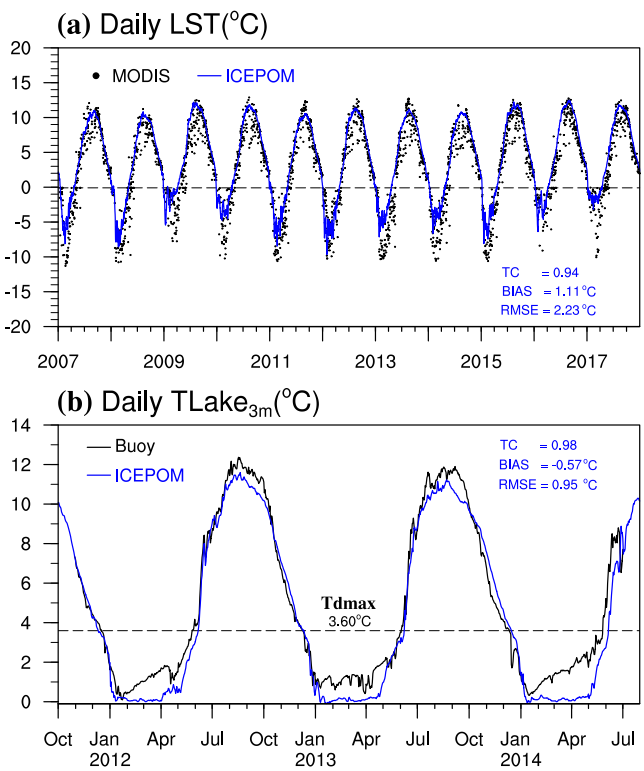

Figure 6. (a) The daily lake-wide averaged LST during 2007–2017 from MODIS observation and ICEPOM simulation. (b) The daily $TLake_{3m}$ from the in situ observation and ICEPOM simulation at the mooring site during October 2011 - July 2014. In (a), the dashed baseline denotes the freezing point of −0.09°C in LNC. In (b), Tdmax denotes the "temperature of maximum water density" and is estimated to be 3.60°C with a pressure of 0.57 bar and a salinity of 1.7 g L^{-1} for LNC.

3.3. Lake Thermal Structure

Figure 8 shows the daily time series of the lake temperature profile at the mooring site from in situ observations and ICEPOM simulation with 1-km spatial resolution during 2012–2013. Here, the onset (end) of warm thermal stratification is defined as the first (last) date during which a temperature difference of 1°C between surface and bottom waters occurs. According to observations (Figure 8a), LNC is thermally uniform till early May, with the lake column temperature below the temperature of maximum water density (Tdmax). Note that Tdmax depends on the surface air pressure and water salinity (Chen & Millero, 1986). It is typically 4°C for freshwater, and is lower for alpine saline lakes, for example, 3.60°C with a pressure of 0.57 bar and a salinity of 1.7 g L^{-1} for LNC (Figure 6b, Wang et al., 2019). With the increase in radiative heating, water in the upper layer is first heated toward Tdmax, and thus becomes denser and mixes with the water beneath. This is known as the spring overturning that has profound biogeochemical impacts by promoting the exchanges of oxygen, nutrients, carbon dioxide, and methane between the epilimnion and hypolimnion (Boyce et al., 1989; Holland & Kay, 2003; Tsydenov et al., 2016). The spring overturning ends until the onset of warm thermal stratification, after which the temperature of mixed layer increases rapidly and the thermocline deepens to more than 30 m.

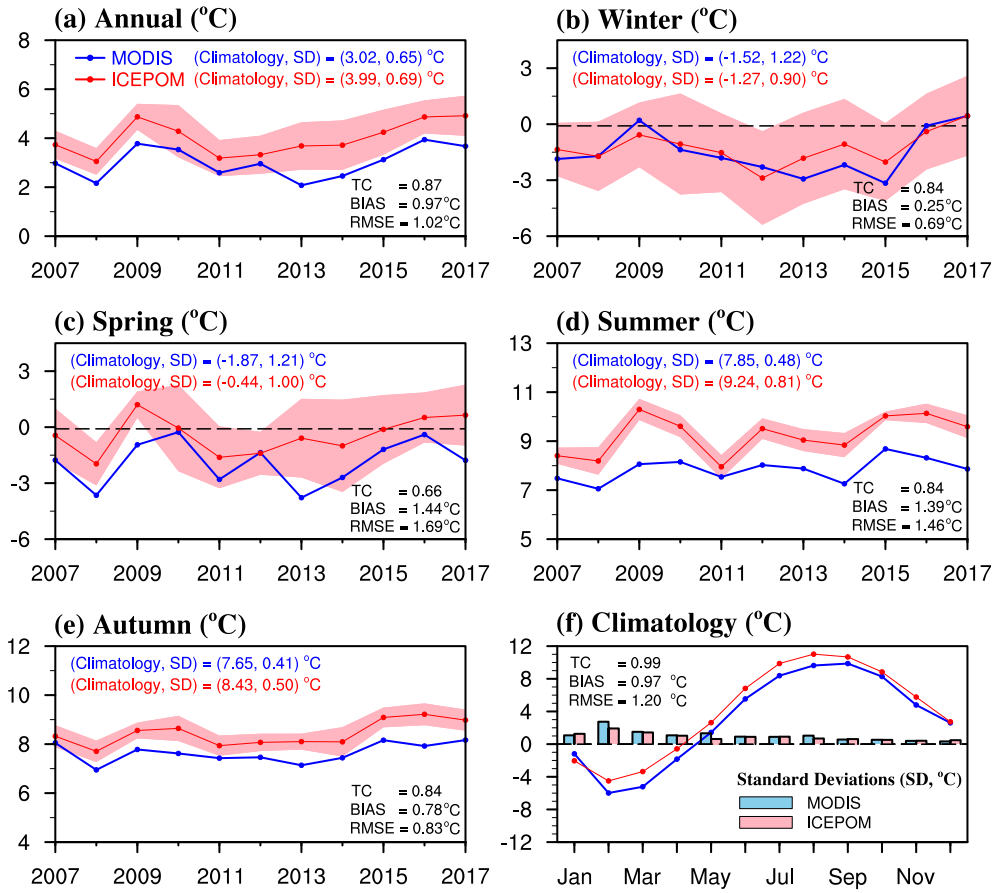

Figure 7. The time series of (a) annual and (b–e) seasonal lake-wide averaged LST during 2007–2017 from MODIS observation and ICEPOM simulation. In (a–e), the blue and red texts denote the climatologically mean LST and their interannual variances defined as the standard deviation (SD) of the respective annual time series, from the MODIS observations and ICEPOM simulations during 2007–2017, respectively. The shaded regions in (a–e) represent the SD of the simulated LST at different model grids across the lake. The dashed baselines in (b, c) denote the freezing point of −0.09°C in LNC. (f) Multi-year means of monthly LST time series, with the bars denoting the SD of respective annual time series for each month.

Destratification starts in September and LNC enters the phase of convective cooling and overturning when LST drops to Tdmax during late autumn. During winter, LNC is ice-covered and a weak inverse thermal stratification forms. ICEPOM reasonably reproduces the seasonal evolution of lake thermal structure. The RMSE values of the water temperature are within the reasonable range of 0.75–1.05°C. The simulated onset, end, and duration of warm thermal stratification during 2012 (2013) are 10th June (11th June), 16th November (15th November), and 160 (158) days, all match well with the 9th June (4th June), 7th November (7th November), and 152 (157) days diagnosed from in situ observations (Table 2).

4. Space-Time Variations of Lake Ice Based on the ICEPOM Simulation

4.1. Seasonal Variations

Figure 9 shows the modeled monthly spatial distribution of ice concentration, thickness, and drift velocity averaged over 2007–2017. During late autumn, the western shallow basin destratifies earlier and cools faster than the mid-lake LNC due to the enhanced prevailing southwesterly (Wu et al., 2021), favoring the formation of supercooled water and thin ice. Wind and wind-induced lake surface waves will act to break up the thin ice and limit its development (Bai et al., 2020), but these processes are not included in ICEPOM. The prevailing strong westerly and the wind-induced currents promote the persistent eastward ice drift during December and January (Figures 9a2 and 9b2). In January, the eastern LNC first becomes ice-covered, and subsequently ice expands from

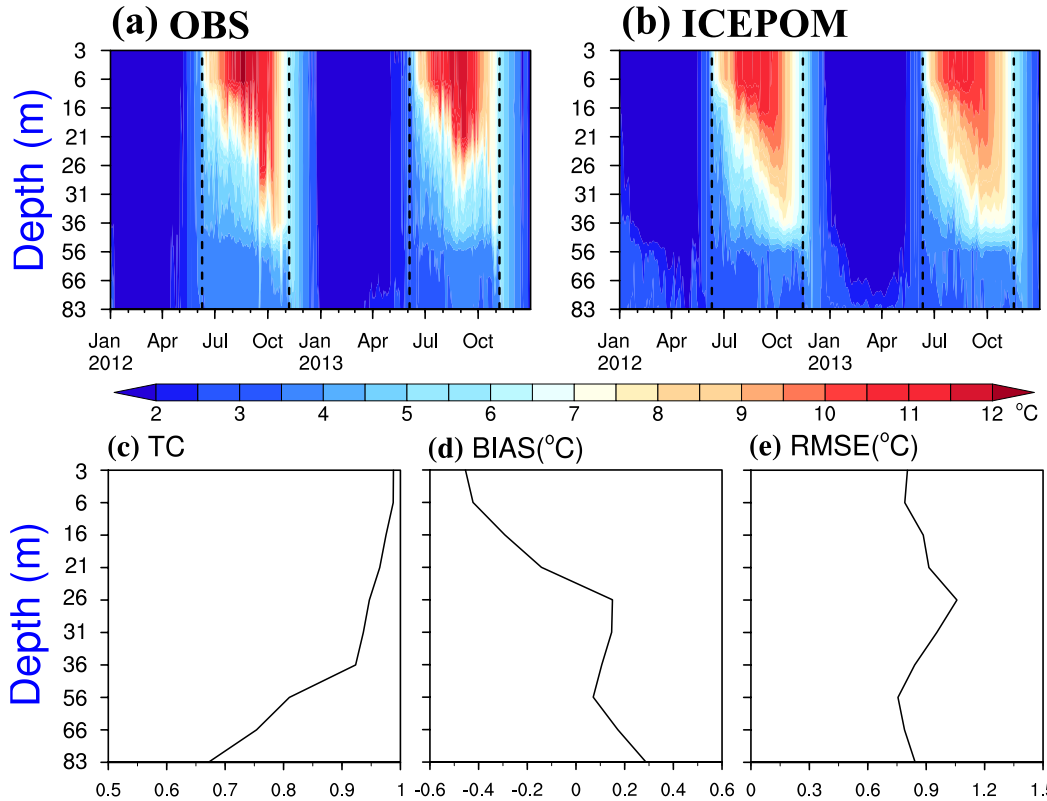

Figure 8. Time-depth distribution of the daily mean water temperature from (a) observations and (b) ICEPOM simulation at the mooring site during 2012–2013. The vertical distributions of the (c) TC, (d) BIAS, and (e) RMSE for the daily water temperature from ICEPOM relative to observations at 10 levels. The black dashed lines in (a) and (b) indicate the onset and end of warm thermal stratification.

east to west during February and March. The ice concentration and thickness are much higher in the eastern LNC than in the western LNC. The lake ice starts to decay in April with a faster rate of ice melting in the western LNC (Figures 9e1 and 9e2). Compared with the central and eastern basins, the ice coverage is much lower and the lake water temperature rises higher in the western LNC following the increasing radiative heating. The prevailing westerly causes eastward ice drift, and also eastward surface current that continuously carries the warm water from west to east. The combined effects cause the whole LNC become ice-free in May (Figures 9f1 and 9f2). Figure 10 shows that, averaged during 2007–2017, the local freezing, thawing, and lateral ice transport all cause much larger changes of effective ice thickness in the eastern than in the western LNC.

According to Figure 9, thinner ice has larger drifting speeds in LNC, thus the drift of thin ice must play a vital role in determining the spatial distribution of lake ice. The drift of thin ice can be induced by both surface wind and current. Here, a multiple linear regression analysis is applied to the daily data when the modeled ice concentration is greater than 5% and effective ice thickness is less than 0.1 m. The criterion is chosen to meet both the thin ice condition and enough samples for performing the multiple linear regression analysis. At a mid-lake location P1 (30.76°N, 90.50°E, marked in Figure 10) with water depth of 95 m, the resulting regression relationship is:

$$\vec{V}_{\text{ice}} = 0.0197e^{i(-19.1^{\circ})}\vec{V}_{w} + 0.2962e^{i(-2.6^{\circ})}\vec{V}_{c} + 0.0085e^{i(-167.7^{\circ})}$$

As presented in Figure 11a, the modeled and regressed ice drift speed have a squared correlation coefficient (R^2) of 0.86 and the regression relationship is statistically significant with $p < 0.001$, according to the F test. The regression relationship suggests that, on average, the wind-induced ice drift has an angle of 19.1° to the right of the wind direction in consistent with the Ekman effect, while the current-induced drift is only at a small angle of 2.6° to the right of

Table 2
The Warm Thermal Stratification Diagnosed From In Situ Observations and ICEPOM Simulations During 2012–2013, With the Model Results Given in Parentheses

	Warm thermal stratification		
Year	Onset	End	Duration (Days)
2012	9th June (10th June)	7th November (16th November)	152 (160)
2013	4th June (11th June)	7th November (15th November)	157 (158)

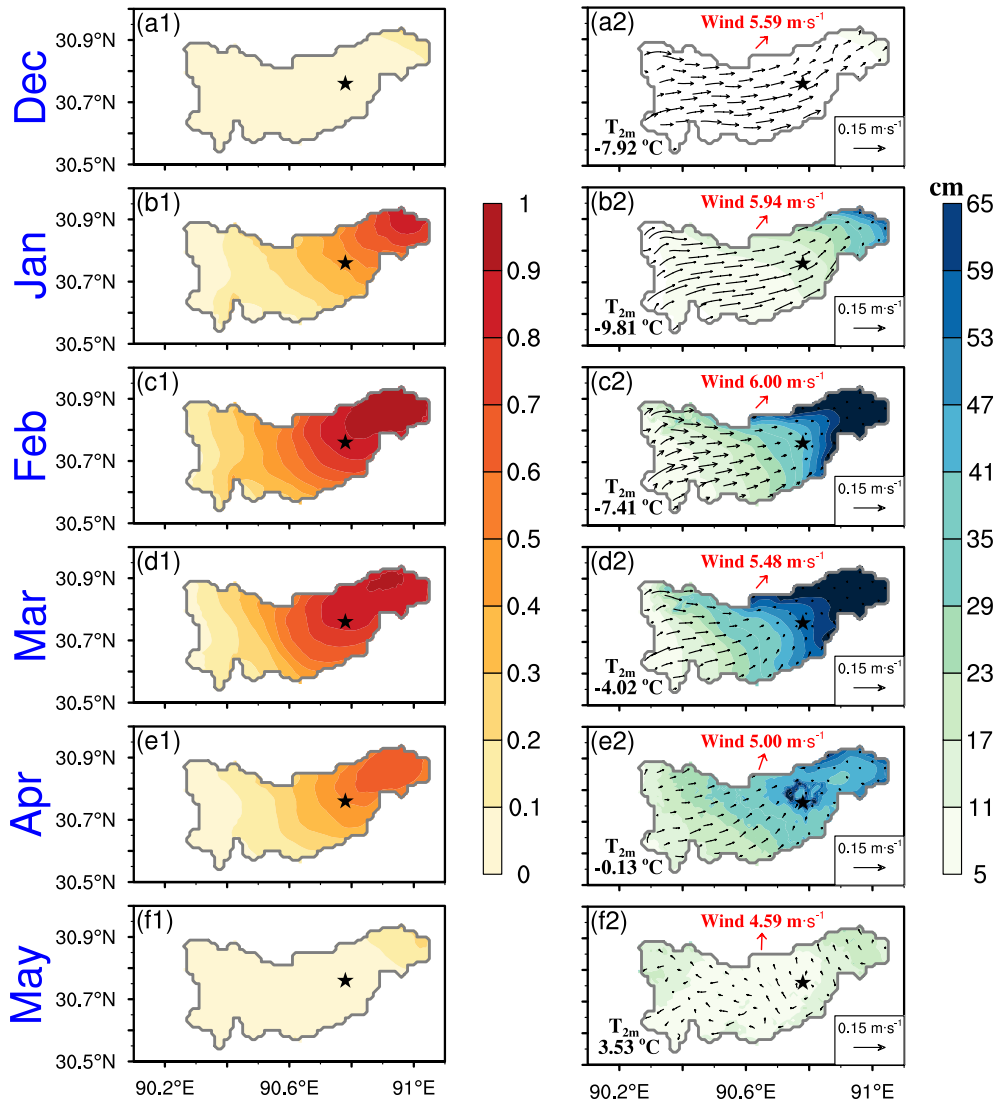

Figure 9. Monthly evolution of modeled lake ice concentration (left column), thickness and drift velocity (right column) during 2007–2017. In the right column, the text in black denotes the lake-wide averaged near-surface air temperature, text and arrows in red denote the lake-wide averaged surface wind. The black stars mark the mooring site.

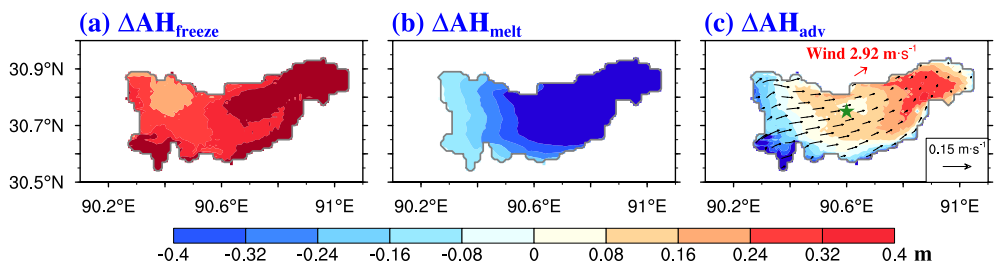

Figure 10. Changes of the effective ice thickness (shaded areas) due to (a) freezing, (b) melting, and (c) advection averaged during 2007–2017. In (c), the vectors denote the ice drift, the text and arrows denote the near-surface wind averaged over December-May in 2007–2017, and the darkgreen star denotes the selected site P1 (30.75°N, 90.60°E), with the water depth of 95 m, for analyzing the key factors of ice drift presented in Figure 11.

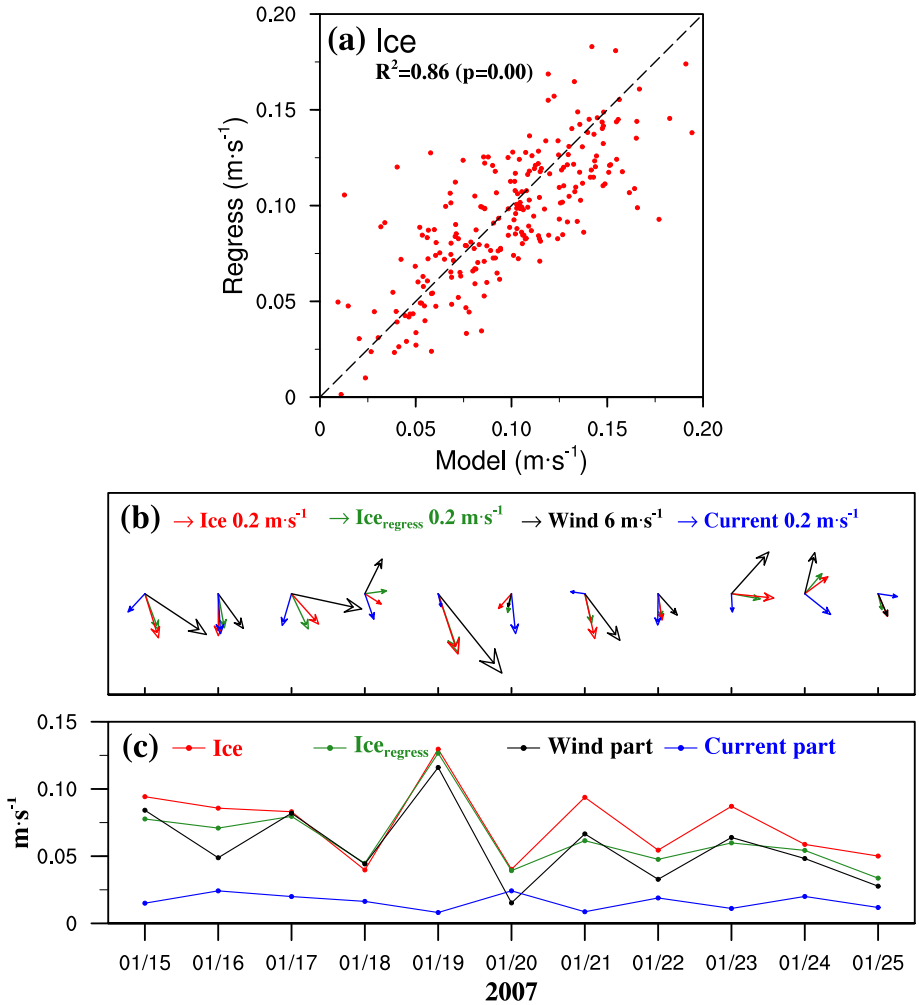

Figure 11. Ice drift at P1 (30.75°N, 90.60°E): (a) the daily ice drift speed from the model versus that from the multiple linear regression during 2007–2017. (b) The daily ice drift during January 15–25, 2007, from the model simulation (red vectors) and multiple linear regression (dark green vectors), as well as surface wind (black vectors) and surface current (blue vectors). (c) The daily ice drift speed from model simulation (red curve) and multiple linear regression (dark green curve), and the regressed contributions from surface wind (black curve) and current (blue curve).

the direction of the current. For the daily values, directions of the modeled ice drift can deviate significantly from that of wind and surface current (Figure 11b). The regressed ice drift speed is mainly due to the contribution of surface wind, instead of due to surface current (Figure 11c). Similar ice-wind-current relationship also holds for other locations in LNC. Hence, we conclude that the prevailing westerly plays a leading role in causing the eastward drift of thin ice, and thus the heavier ice coverage in the eastern LNC. This corresponds to the field observations of thick superimposed ice consisting of two or more ice layers along the southeastern shore (Qu et al., 2012).

4.2. Interannual Variations

Beside the distinct seasonal cycle, the ICEPOM results also show substantial interannual variations of ice in LNC. Figure 12 shows the monthly spatial distributions of the effective ice thickness and drift velocity from the preceding December to May in 2011 and 2017, respectively. Evidently, the ice condition is much lighter in the winter of 2017 than in 2011, corresponding to the lake-wide averaged T_{2m} contrast of −3.12 versus −5.65°C for the whole winter. Compared with 2011, the lake ice forms later and melts earlier in the winter of 2017, with 103 days of ice-covered duration, 25 days shorter than 128 days in 2011. The ice extent and thickness during February–April in 2017 are also greatly reduced than in 2011. The eastward drift of thin ice is more widespread in 2017 than in 2011.

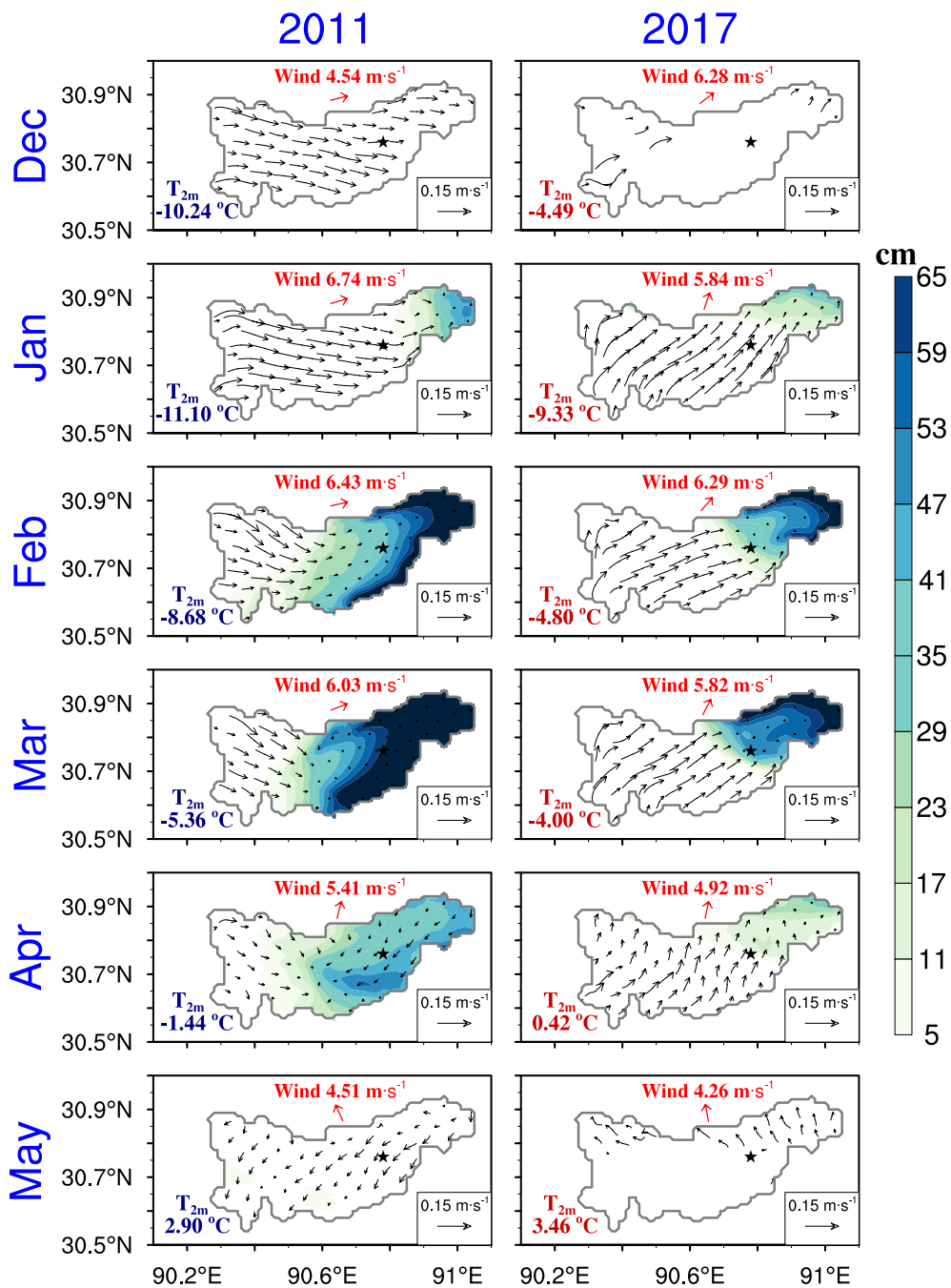

Figure 12. Spatial distributions of the effective ice thickness and drift velocity from ICEPOM during the preceding December to May in 2011 and 2017. The format is the same as the right column of Figure 9.

Variations of the lake-wide averaged ice area and volume from ICEPOM and the over-lake T_{2m} during 2007–2017 are presented as daily times series (Figures 13a and 13b), the monthly climatology and the standard deviations of the respective annual time series for each month (Figures 13c and 13d). Variations of ice area and volume, at both seasonal and interannual time scales, well track each other. The ice-on date, maximum ice volume and ice-off date have evident time lags relative to when T_{2m} drops below T_{frz}, reaches minimum, and rises above T_{frz}, respectively. This is evident in their seasonal cycles (Figures 13c and 13d). That is, in December the ice volume is still small although T_{2m} has dropped to well below 0°C; the ice volume peaks in March behind the minimum T_{2m} in January; and the ice volume diminishes in May while T_{2m} rises near 0°C in April. The over-lake T_{2m} has larger interannual standard deviations in winter months of December, January and February, than in spring months of

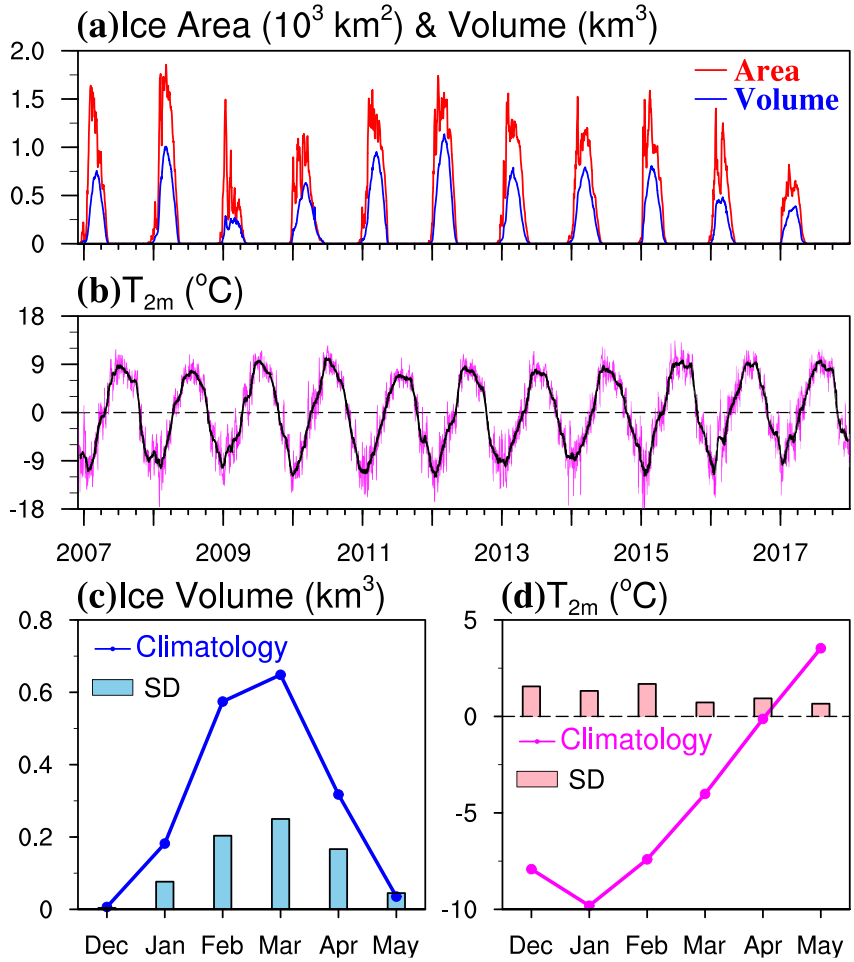

Figure 13. (a) Daily time series of lake-wide averaged ice area (red curve) and volume (blue curve) during 2007–2017 from ICEPOM. (b) Daily time series of lake-wide averaged over-lake T_{2m} (magenta curve), overlaid with 30-day running means (black curve). The monthly (c) ice volume and (d) over-lake T_{2m} averaged during 2007–2017, with the bars denoting the standard deviation (SD) of the respective annual time series for each month.

March, April, and May. In contrast, the ice volume has larger interannual standard deviations in February, March and April, than in December, January and May. The seasonal phase relationship between the ice volume and T_{2m}, including their seasonal cycles and the occurrence of stronger interannual variability, is due to the "cumulative effects" of T_{2m} in preceding months to be presented in Figure 14.

Figure 14 shows the annual time series of the lake-wide averaged ice volume, duration, and ice-on and ice-off dates. The ice-on (ice-off) date at each grid point *i* is defined as the first (last) date when the effective ice thickness is above (below) 0.01 m, and the ice duration is the total number of days between them. During 2007–2017, the mean values of ice volume, ice duration, ice-on date, and ice-off date are 0.73 km^3, 152 days, 13th December, and 13th May, respectively. All these parameters show substantial interannual variations and evident correlations with each other. That is, higher ice volume usually corresponds to longer duration, earlier ice-on, and later ice-off dates. Compared to the mild winter of 2017, the ice volume in the severe winter of 2012 increases by 2.4 times from 0.39 to 0.95 km^3, the ice-on date advances by 18 days from 30th December to 12th December, the ice-off date delays by 17 days from 5th May to 22nd May, and the ice duration extends by 35 days from 127 to 162 days. Since 2011, the ice parameters show evident trends featured by decreasing ice volume, delaying of freezing, advancing of thawing, and shortening of ice duration. The ICEPOM simulated interannual variations of lake ice phenology during 2007–2017 are similar with that based on analyses of satellite remote sensing data (Gou et al., 2017; Guo et al., 2020). The magnitudes of interannual variations during 2007–2017 are larger than during the longer time series of 1978–2017 analyzed by Guo et al. (2020), and 2000–2015 analyzed by Gou et al. (2017).

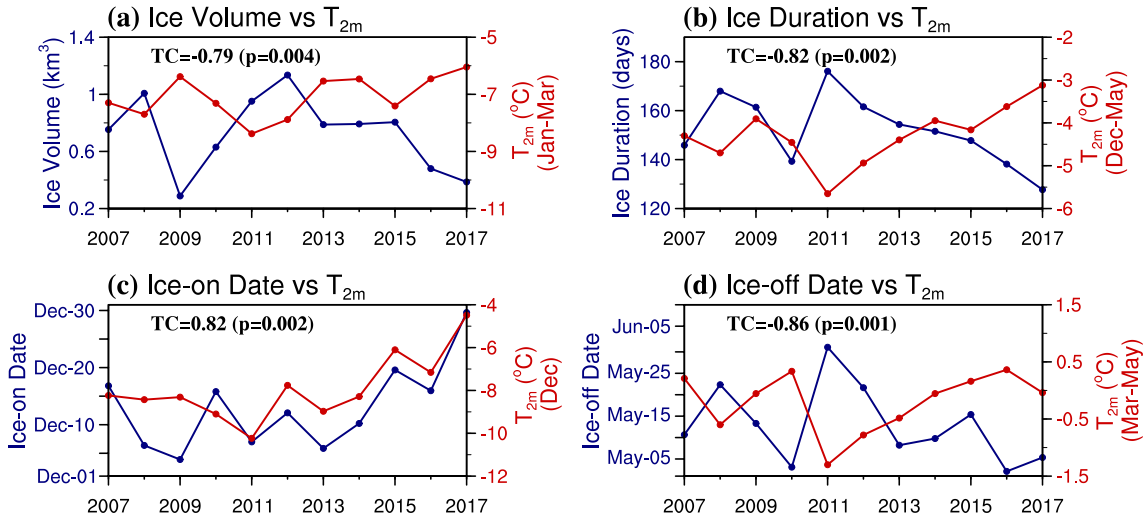

Figure 14. The annual time series of lake-wide averaged (a) ice volume, (b) ice duration, (c) ice-on date, and (d) ice-off date from ICEPOM during 2007–2017 (blue curves), overlaid with the over-lake T_{2m} (red curves) during (a) January-March, (b) preceding December to following May, (c) December, and (d) March-May.

The "cumulative effects" of T_{2m} on ice variations have been analyzed in previous studies. For example, Ashton (1989) and Yu et al. (2014) found that the cumulative freezing (CFDD) or thawing (CTDD) degree days, calculated as the integral of $T_{2m} - T_{\text{frz}}$ over different preceding months, have strong correspondence with the ice phenology. For LNC, the CFDD from December to the following March is calculated according to $\int_{\text{December}}^{\text{March}} \min(T_{2m} - T_{\text{frz}}, 0)dt$, where T_{frz} is set as −0.09°C. The resulting annual time series of CFDD has a high TC value of −0.81 with the annual time series of maximal ice volume. We also quantify the "cumulative effects" by simply averaging T_{2m} over different preceding months, with the resulting interannual time series correspond to that of different ice parameters shown in Figure 14. It is found that the lake-averaged ice volume has a high value of TC = −0.79 with T_{2m} averaged over the ice formation months of January–March (Figure 14a); the ice duration has TC = −0.82 with T_{2m} averaged over the whole winter from the preceding December to May (Figure 14b); the ice-on date has TC = 0.82 with T_{2m} in December when ice starts to freeze (Figure 14c); and the ice-off date has TC = −0.86 with T_{2m} averaged over March–May (Figure 14d).

Lastly, we examine the variations of the lake-wide averaged ice drift. Figures 15a and 15b show the ICEPOM simulated 5-day running mean ice drift speed (WS_i) and the eastward (U_i) and northward (V_i) components of ice drift velocity. Figures 15c and 15d show the monthly values of these three parameters averaged during 2007–2017, as well as the standard deviations of the respective annual time series for each month. The ice drift shows strong variability at short (weather band) and seasonal time scales. As discussed in Section 4.1, variations of thin ice drift at daily time scale are mostly due to wind. For the seasonal cycle, there is high correspondence between the evolution of ice drift with that of ice volume (Figures 9 and 12) and lake surface wind (Figure 3). In December and January, WS_i, U_i, and V_i reach values of 0.10, 0.06, and 0.02 m·s^{-1}, corresponding to smaller ice volumes and stronger winds with daily speed up to 8 m·s^{-1}. The northeastward drift of thin ice is consistent with the direction of the southwesterlies, on average. During February and March, the mean WS_i, U_i, and V_i are reduced to 0.07, 0.03, and 0.01 m·s^{-1}. The reduction of over-lake averaged ice drift can be mostly explained by the slow drift of thick ice in the eastern LNC (Figure 9), and also the reduction of wind speed. In April and May, the mean WS_i rises to 0.07 m·s^{-1}, which must be due to the reduction in ice volume (thickness) because the wind further weakens compared with February and March. Note that May is the only month when the northward V_i is larger than the eastward U_i, consistent with the direction of prevailing weak southerly (Figure 3e). The interannual variation of ice drift in different months has similar standard deviations. This may be due to the combined effects of variations in wind and ice volume, based on the mean ice drift variations discussed above.

5. Discussions

5.1. Comparison With One-Dimensional Lake Model Simulations

In previous studies, 1-D lake models, for example, the 1-D lake component from the Weather Research and Forecast Model (WRF-Lake), have been extensively used in simulating the thermodynamics of TP lakes. While the

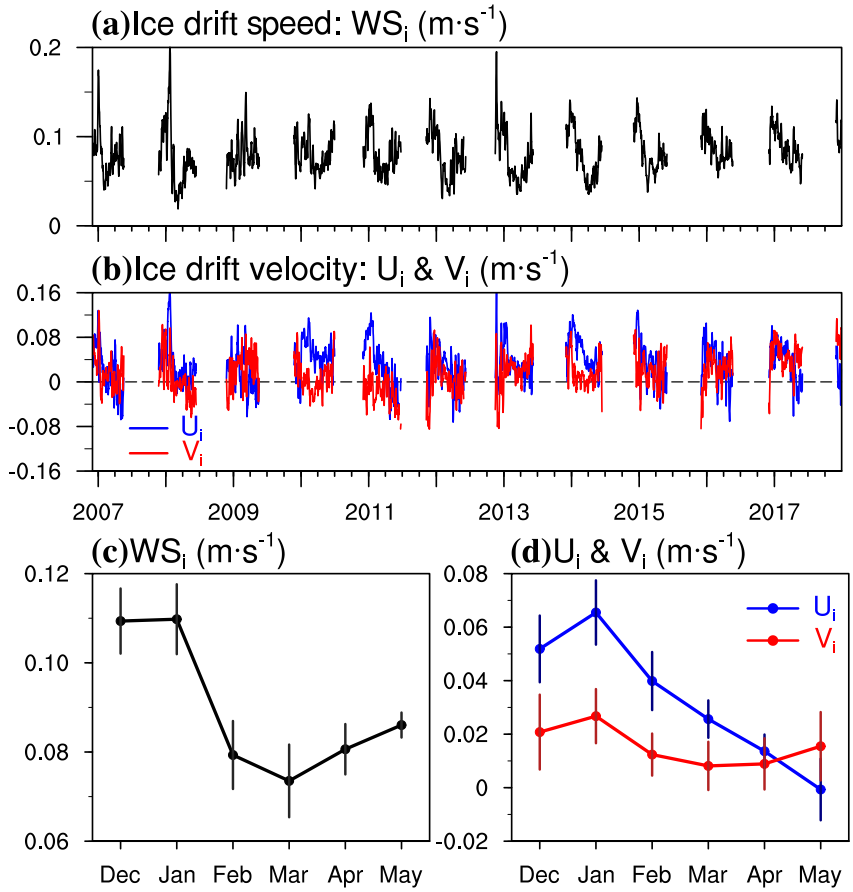

Figure 15. ICEPOM simulated 5-day running mean time series of the lake-wide averaged (a) ice drift speed (WS_i), and (b) the eastward (U_i) and northward (V_i) components of ice drift velocity during 2007–2017, and the monthly (c) ice drift speed and (d) eastward/northward ice drift velocity averaged during 2007–2017, with the bars denoting the standard deviation of the respective annual time series for each month.

1-D lake models are computationally efficient and work well in simulating the lake-wide averaged LST through a series of parameter tuning, certain deficiencies exist in reproducing the spatial variability of large-lake thermodynamics due to the unresolvable lateral processes (Wu et al., 2021; Xue et al., 2017). Figure 16 compares the monthly spatial distributions of lake ice from ICEPOM and the simulations with the 1-D lake component of WRF-Lake during the preceding December to May in 2013. The 1-D model is run on each horizontal grid of ICEPOM using the same initial condition and surface forcing, hence it also obtains a spatially varying ice condition. Compared with the ICEPOM solution, 1-D model obtains no obvious contrast between the ice coverage in western and eastern LNC, due to the lacking of eastward advection of thin ice. The 1-D model solution shows thinner ice in the central LNC than in coastal waters. This can be explained by the variations of lake water heat content that depends on water depth. In the shallow coastal areas, the water temperature drops faster in late autumn and ice first appears there in December and further increases rapidly in January. Overall, the spatial distribution of ice from the 1-D model shows little resemblance of that from satellite observations (Figure 4).

5.2. Role of Ice Dynamics in Determining the Ice Variations

The evolution of ice thickness distribution is essentially determined by three parts: (a) thermodynamic process related the surface, bottom, and lateral heat fluxes; (b) horizontal advection; and (c) mechanical redistribution due to convergence, divergence, and shear (Hibler, 1979, 1980; Thorndike et al., 1975). To assess the importance of ice dynamics (including (b) and (c)) in simulating the ice variations, we perform a sensitivity experiment with the ice dynamics in ICEPOM turned off (Exp_sen), but otherwise the same as the full run described in Section 2.3. Figure 17 shows the monthly spatial distribution of ice concentration and thickness during 2007–2017 from Exp_sen. Compared with the solution with ice dynamics (Figure 9),

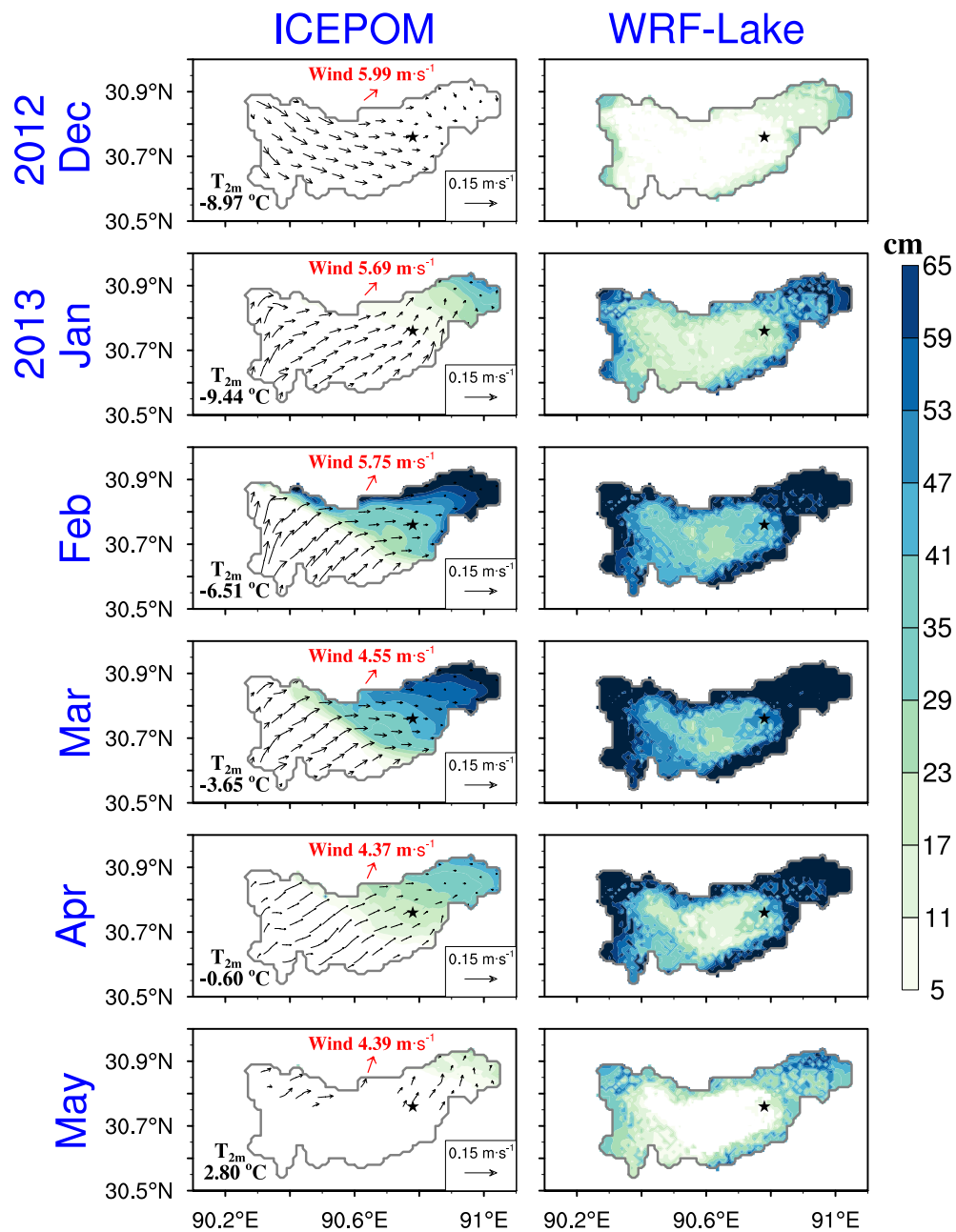

Figure 16. Left: Same as Figure 12 but for the ICEPOM simulation during the preceding December to May in 2013. Right: Ice thickness from the simulation with WRF-Lake.

Exp_sen obtains evidently higher ice concentration and thickness in the western LNC, thinner ice in the eastern LNC, and fails to capture the seasonal evolution of the ice freezing/melting processes discussed in Section 3.1. The differences between full run and Exp_sen can also be seen through comparing the simulation results with satellite-derived freezing/melting processes in 2012 and 2014 (Figures S1 and S2 in Supporting Information S1). This suggests the necessity of including ice dynamics, for example, the eastward ice drift, the creation of open water and ridging during ice convergence, to simulate the spatiotemporal variations of ice in LNC. In previous coupled atmosphere-hydrodynamic ice modeling studies of Laurentian Great Lakes, Xue et al. (2017) and Sun et al. (2020) turned off the ice dynamics for the sake of computational efficiency. This treatment in these modes still led to credible results of lake-wide averaged ice cover and LST due to the dominance of ice thermodynamic variation. However, excluding the ice dynamics in simulations of large lakes, as

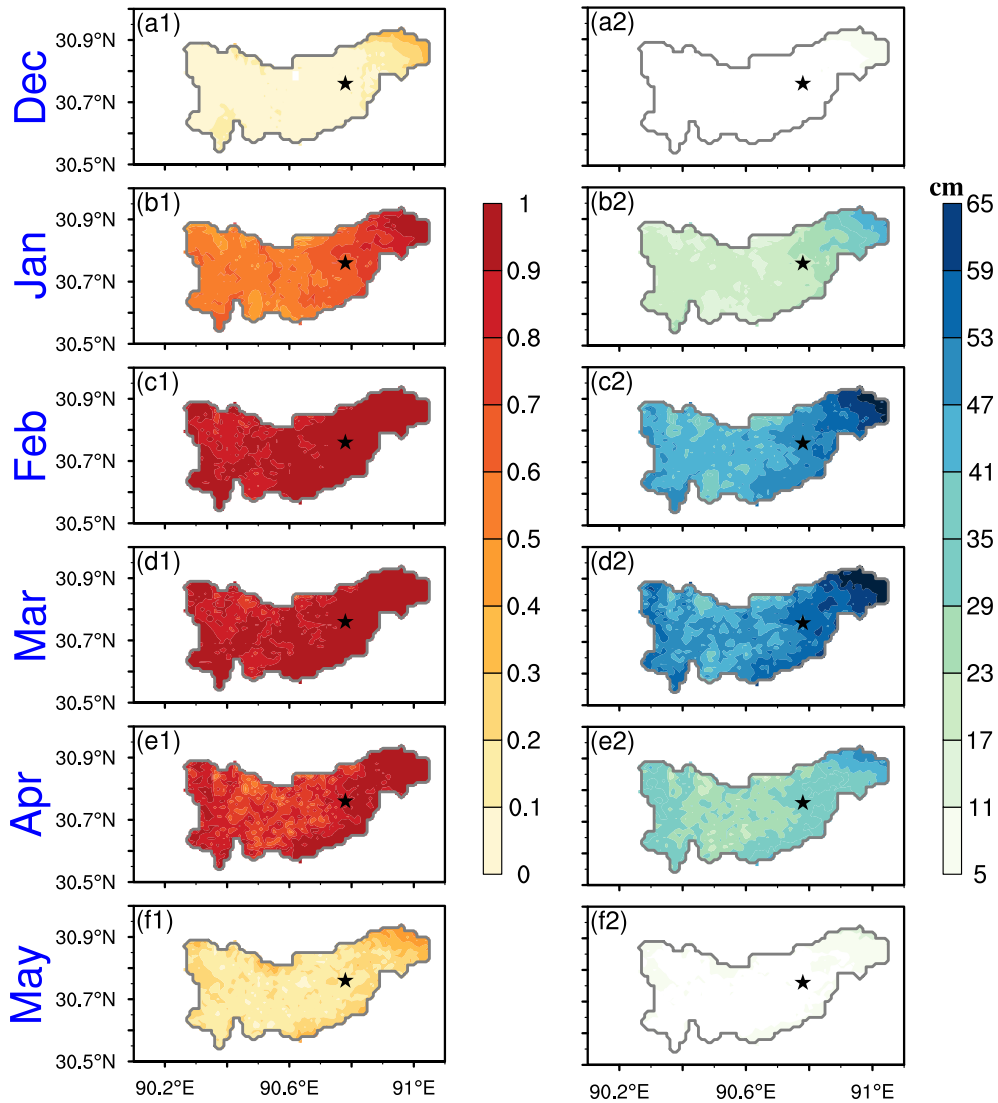

Figure 17. Same as Figure 9 but for the ICEPOM simulation with the ice dynamics turned off, hence without ice drift to be presented.

demonstrated with the results of Exp_sen in LNC, creates incorrect representation of ice distribution and thus the related surface energy fluxes. The potential impacts on coupled simulations deserve further investigation.

5.3. Comparison Between the Ice Coupled and Uncoupled Simulations

The application of ICEPOM enables the multi-year simulation of ice and thermo-hydrodynamic variations in LNC, thus extends the previous study of Wu et al. (2021) who only simulated the ice-free seasons of 2013 using the 3D thermo-hydrodynamic model POM without the ice component. A preliminary analysis shows that for the ice-free seasons of 2013, ICEPOM and POM obtain similar characteristics of space-time variations of lake circulation and water temperature, but with evident quantitative differences. These differences are partially related to changes in model settings, for example, the regression formula applied to adjust the CMFD wind speed and the bulk aerodynamic formula for surface turbulent heat flux, and are partially related to with or without the influence of ice at the start of the ice-free season. To further demonstrate the added value of ice coupling in simulating the lake thermo-hydrodynamics, a pair of model sensitivity experiments are carried out using ICEPOM, one with the ice component included (Exp_ice), and one with the ice component turned off but with a necessary constraint that the water temperature is not allowed to drop below the freezing point (Exp_noice). Both simulations start from 20 May 2011 with a uniform water temperature of 2.24°C, and all the other parameters the same

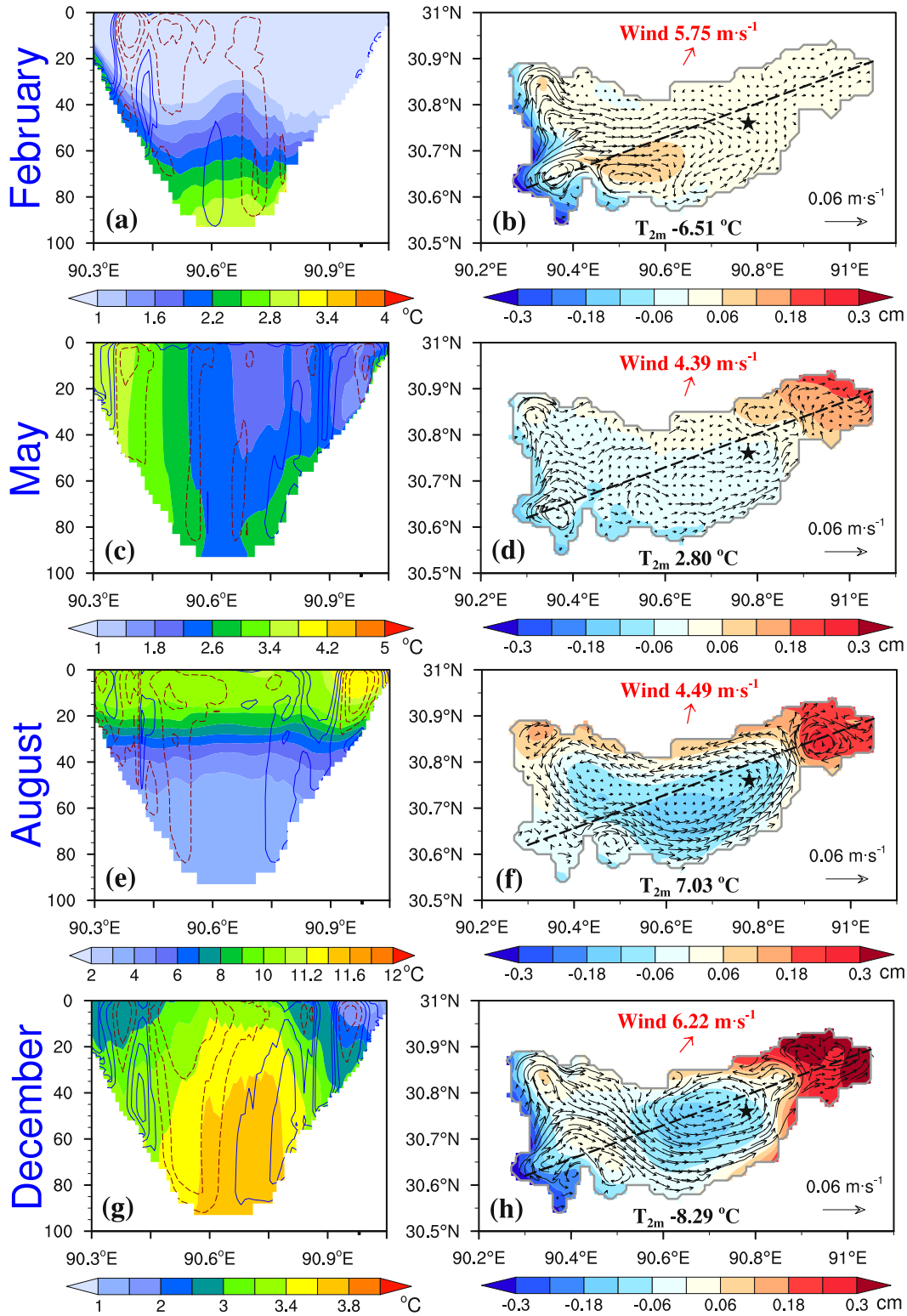

Figure 18. ICEPOM simulation with the ice component included (Exp_ice) starting from 20 May 2011: Monthly averaged (left column) lake temperature (color shading) along and horizontal currents (contours) normal to a southwest-northeast transection, and (right column) horizontal distributions of water level (color shading) and depth-averaged currents (vectors) in February, May, August, and December 2013. In the left panels, the contours have intervals of 0.01 $m \cdot s^{-1}$, with solid (dashed) contours denoting northwestward (southeastward) currents. In the right panels, the black dashed lines denote the transection position, and the formats of stars, texts, and arrows are the same as the right column of Figure 4.

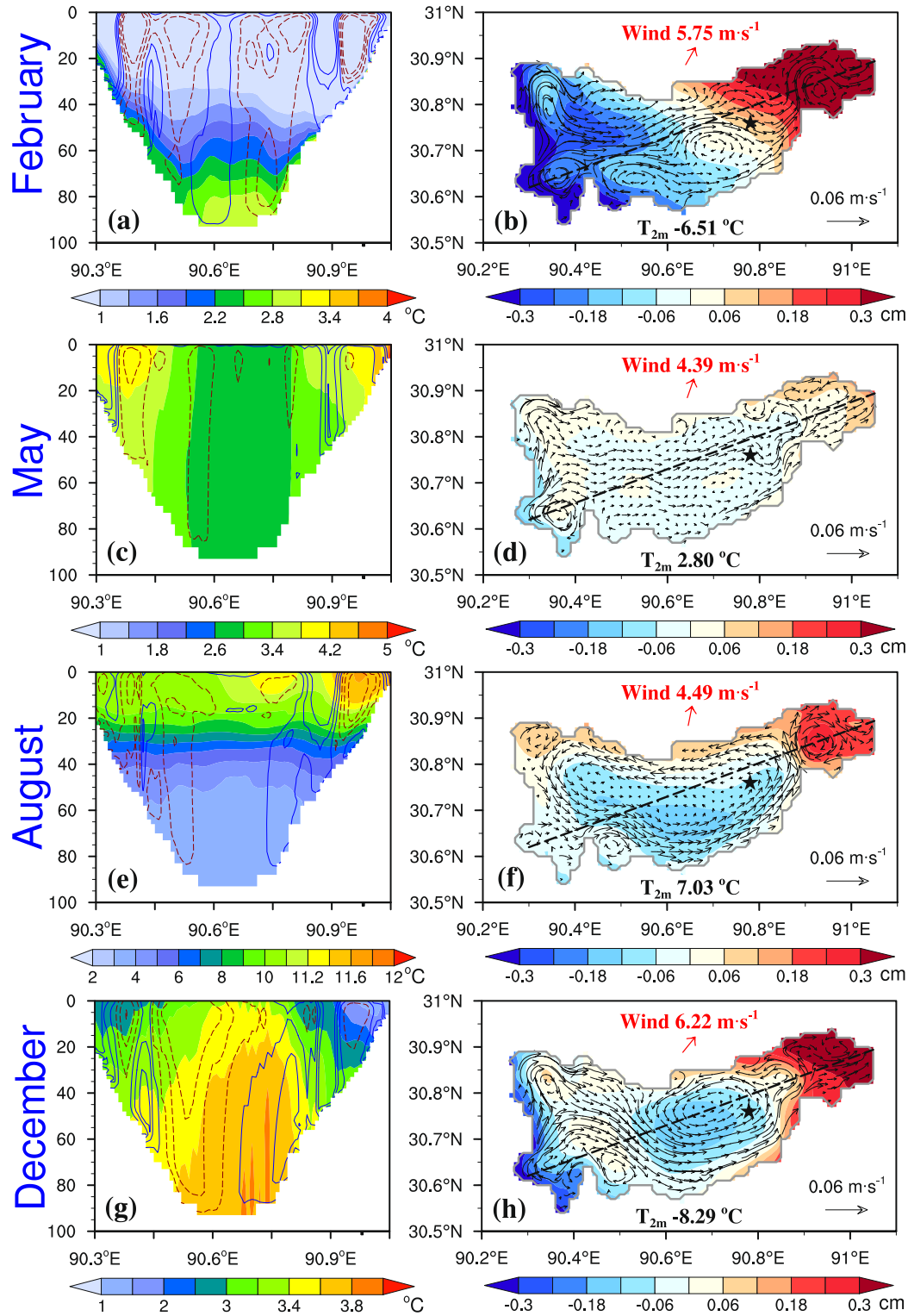

Figure 19. Same as Figure 18 but for the ICEPOM simulation with the ice component turned off (Exp_noice).

as the main ICEPOM simulation started on 20th May 1999 and end on 31 December 2014. Figures 18 and 19 show the simulated water temperature along a southwest-northeast transection, and the horizontal distribution of the depth-averaged water currents and level in February, May, August, and December 2013. The two solutions are distinctly different in February when Exp_ice obtains much weaker lake circulation and water level gradient over the whole lake, and in May when Exp_ice obtains lower water temperature in the central and eastern parts of the lake. In both months, the differences between the two solutions can be explained by the impacts of ice in limiting the water movements and spring radiative warming that are included in Exp_ice but not in Exp_noice. In August and December, the two solutions are quite close to each other. This suggests that the added value of including the ice component lies mainly in winter and spring with the presence of ice, instead of in summer and autumn.

5.4. Model Limitations

Despite the successful initial application of ICEPOM on a typical large lake over TP, the model results also indicate various processes and natural phenomena which are not parametrized or well reproduced by the model.

First, different ice cover compositions, for example, snowpack, snow ice and transparent ice, cause different ice physical properties (e.g., albedo, transparency and thermal conductivity) which greatly influence the atmosphere-ice-water energy interaction and thus the ice phenology (Brown & Duguay, 2010; Kirillin et al., 2012). For example, due to the insulation effects of snowpack and snow ice, the bulk of thicker ice in high-latitude lakes presents toward the end of ice season and then rapidly melts (Brown & Duguay, 2011). However, the present ICEPOM does not take account of snow accumulation and adopts the assumption of uniform ice cover composition. This may explain the nearly symmetric ice thickness-duration curve predicted by the model (Figure 5). Moreover, according to the ice phenology derived from multiple MODIS data sets during 2000–2015, LNC froze up from east to west, with the eastern LNC freezing up in early January and breaking up in May, the central LNC freezing up in late January and breaking up since April, and the western LNC freezing up in February and breaking up in late March. LNC was totally ice-covered since February except for the winters of 2002 and 2009, and various melt-refreeze events occurred in the western LNC during the winters of 2003, 2004, and 2006 (Gou et al., 2017). ICEPOM reasonably reproduces the seasonal evolution of lake ice, but fails to capture the nearly complete ice coverage (Figures 4, 9, and 12). The modeled ice thickness and cover in the western LNC are lower than the observed conditions, and the wind-driven eastward ice drift and accumulation may be overestimated. Because the snowpack and snow ice generally reduce the absorption of solar radiation and favor the ice growth, implementation of snow processes is an urgent task for accurately reproducing the spatiotemporal variations of lake ice in LNC. Coupling a mechanical deformation model (e.g., Thorndike et al., 1975) is another necessary model improvement that may resolve the excessive ice accumulation in the eastern LNC.

Second, the present ICEPOM solution shows obvious errors in reproducing the water temperature during the ice-covered phase. This requires further investigation the model representation of under-ice processes, for example, the heat exchange between the deep layer and the bottom sediments (Mortimer, 1971; Mortimer & Mackereth, 1958), and the radiatively driven convection especially during the ice-melting phase (Jonas et al., 2003; Mironov et al., 2002).

Finally, we note the importance of improving the surface forcing fields. More in situ observational data are required to evaluate or correct the CMFD or other surface forcing data products. With respect to surface wind, the simple scaling of the CMFD wind speed with $Y = 1.17X + 1.62$ is potentially a source of bias in the present simulation, as previous studies (Beletsky et al., 2013; Xue et al., 2015) have pointed out the importance of accurate representation of the over-lake wind amplitude and the mesoscale spatial variability for lake thermo-hydrodynamic simulations. Katabatic winds are potentially induced from the altitude difference between LNC (~4,730 m) and the nearby Nyainqentanglha Mountains (~6,000 m), and the impacts of such winds deserve further study. Besides the meteorological data, more comprehensive in situ observational data sets, including ice thickness/composition, snow depth, water temperature and currents, etc., are also highly desirable for surface forcing adjustment, model validation and improvement.

6. Conclusion and Recommendations for Future Studies

In this study, a 3-D lake-ice coupled model is for the first time applied to investigate the space-time variations of ice and the underlying mechanisms in LNC during 2007–2017. The validation shows that ICEPOM reasonably

reproduces the lake ice thickness and vertical water thermal structure from in situ observations, and the ice coverage and lake surface temperature in the horizontal plane based on satellite remote sensing. Complementing field observations and satellite remote sensing, the modeling work helps to provide a more comprehensive view of ice variations at higher resolutions and to discover the underlying mechanisms.

Seasonally, lake ice first appears in the eastern LNC during early January, then expands to the western LNC during February, covers nearly the entire lake in March, retreats from west to east since April, and eventually disappears in May. The eastward drift of thin ice throughout the ice-covered phase and the eastward water heat transport in the ice melting phase are responsible for the spatial variation of lake ice and thus the freeze-thaw processes. The results of multiple linear regression suggest that the daily drift of thin ice is mainly determined by the surface wind, with an acute drift angle to the right of wind direction, while the current-induced drift is much smaller and nearly aligns with the current direction.

Lake ice area, volume, duration, ice-on date and ice-off date show significant interannual variations, which are closely related to interannual variations of the over-lake T_{2m}. Specifically, interannual variations of ice volume, duration, and ice-on and ice-off dates have high correlations with T_{2m}, averaged over January-March, from the preceding December to May, in December and over March-May, respectively. We identify this as the dependence of different ice parameters to the "cumulative effects" of surface air temperature over different preceding months. Note that over the TP lakes, solar radiation does not dimmish even in winter, thus the surface air temperature is below T_{frz} during the ice-freezing and melting phases (while close to T_{frz} at high latitudes; Leppäranta & Wen, 2022). Thus, the variations of ice-on date and ice-off date also correspond to changes of critical values of the surface air temperature for the ice to freeze or melt, which can be related to the amount of solar radiation that the lake or ice receives before the freezing or melt. The other factors (i.e., snow accumulation, wind speed, thermal reserve built up during summer, the accumulated ice volume during winter) are also responsible for the variations of ice phenology (Ashton, 2007, 2011), and deserve future study. Finally, our analysis suggests that the seasonal and interannual variations of ice drift are attributed to the combined effects of wind and ice volume variations.

According to Kirillin et al. (2021), TP lakes store heat during the ice-covered phase. Once the lake ice breaks up, there occurs quick release of heat to the atmosphere in 1–2 days, with the upward heat flux reaching 500 $\mathrm{W{\cdot}m^{-2}}$, favoring the over-lake atmospheric convective activities. Obviously, as 3-D models like ICEPOM obtain more realistic space-time variation of ice, they have more advantages than 1-D models in coupling with atmospheric models to study and predict the regional weather over and around large TP lakes.

Ice extent and thickness in LNC are much smaller in mild winters than in severe winters. The decreased ice cover favors more effective driving of lake circulations by wind, and also intensified lake-air interactions (Fujisaki et al., 2013). The lake is expected to experience stronger radiative heating due to the prolongation in the open-water phase and earlier onset of warm thermal stratification. The influence of radiative heating may be especially crucial for the TP lakes which are exposed to much stronger radiation due to the reduced atmospheric density and optical thickness compared with the plain lakes located in mid-latitude regions (Kirillin et al., 2021; Su et al., 2019; Wen et al., 2016). The above thermo-hydrodynamic variations have far-reaching ecological impacts by determining the distribution and transport of heat, light, oxygen, and nutrients within lakes (Anslan et al., 2020), and may result in potential shifts in thermal habitats for species (Kraemaer et al., 2021). In addition to the thermo-hydrodynamic and ecological impacts, the declined ice cover and the related lake warming also have important feedback on the regional weather and climate via intensified lake-air interactions (Thiery et al., 2016; Woolway et al., 2020). For example, due to the accelerated ice melting over past decades, the surface water in Lake Superior warms faster than the over-lake air (Desai et al., 2009). The decreased temperature gradient between water and air tends to destabilize the atmospheric boundary layer, results in enhanced over-lake wind, and in turn leads to more energetic current and material transport. In the future, ICEPOM could be coupled with atmospheric and ecological models to explore these processes. This is valuable in deepening the understanding of the large-lake processes over TP and their roles in regional climate change, providing scientific support for improving weather forecasting and protecting the aquatic environment.

Data Availability Statement

The field observed bathymetry, LST, ice thickness, and meteorological parameters of LNC (Qu et al., 2012; Wang, 2020; Wu, 2018), and the China Meteorological Forcing Data set (He et al., 2020) are available on the National Tibetan Plateau Data Center. The integrated data set of daily lake surface temperature for 160 lakes over TP is publicly released by Guo et al. (2021). The MOD09GQ surface reflectivity images (Vermote & Wolfe, 2015) can be retrieved through the Google Earth Engine platform (Kumar & Mutanga, 2019). We acknowledge the use of NCAR Command Language version 6.6.2 (The NCAR Command Language, 2019) to analyze model results and plot all the figures.

Acknowledgments
This study is supported by National Natural Science Foundation of China under Grants 41975081, 41975130, 42305015, the bilateral research project GZ1259 of the Sino-German Center for Research Support, CAS "Light of West China" Program (E129030101), the basic research fund of CAMS (2023Y012), the research project of Jiangsu Meteorological Bureau (KQ202313), the Research Funds for the Frontiers Science Center for Critical Earth Material Cycling Nanjing University, the Fundamental Research Funds for the Central Universities (020914380103), the Jiangsu University "Blue Project" outstanding young teachers training object, the Fundamental Research Funds for the Central Universities and the Jiangsu Collaborative Innovation Center for Climate Change. We thank the three anonymous reviewers for their detailed, insightful and constructive comments that help us greatly in revising the originally submitted manuscript.

References

Anslan, S., Rad, M. A., Buckel, J., Galindo, P. E., Kai, J., Kang, W. G., et al. (2020). Reviews and syntheses: How do abiotic and biotic processes respond to climatic variations in the Nam Co catchment (Tibetan Plateau)? *Biogeosciences*, *17*(5), 1261–1279. https://doi.org/10.5194/bg-17-1261-2020

Ashton, G. D. (1989). Thin ice growth. *Water Resources Research Series*, *25*(3), 564–566. https://doi.org/10.1029/WR025i003p00564

Ashton, G. D. (2007). Ice in lakes and rivers. *Encyclopedia Britannica*. https://www.britannica.com/science/lake-ice

Ashton, G. D. (2011). River and lake ice thickening, thinning, and snow ice formation. *Cold Regions Science and Technology*, *68*(1–2), 3–19. https://doi.org/10.1016/j.coldregions.2011.05.004

Austin, J. A., & Colman, S. M. (2007). Lake Superior summer water temperatures are increasing more rapidly than regional air temperatures: A positive ice-albedo feedback. *Geophysical Research Letters*, *34*(6), L06604. https://doi.org/10.1029/2006GL029021

Bai, P., Wang, J., Chu, P., Hawley, N., Fujisaki-Manome, A., Kessler, J., et al. (2020). Modeling the ice-attenuated waves in the great lakes. *Ocean Dynamics*, *70*(7), 991–1003. https://doi.org/10.1007/s10236-020-01379-z

Bai, Z. H., Wang, J., Sellinger, C., Clites, A., & Assel, R. (2012). Interannual variability of Great Lakes ice cover and its relationship to NAO and ENSO. *Journal of Geophysical Research*, *117*(C3), C03002. https://doi.org/10.1029/2010JC006932

Beletsky, D., Hawley, N., & Rao, Y. R. (2013). Modeling summer circulation and thermal structure of Lake Erie. *Journal of Geophysical Research*, *118*(11), 6238–6252. https://doi.org/10.1002/2013JC008854

Biermann, T., Babel, W., Ma, W. Q., Chen, X. L., Thiem, E., Ma, Y. M., & Foken, T. (2014). Turbulent flux observations and modelling over a shallow lake and a wet grassland in the Nam Co basin, Tibetan Plateau. *Theoretical and Applied Climatology*, *116*(1–2), 301–316. https://doi.org/10.1007/s00704-013-0953-6

Birge, E. A. (1910). The apparent sinking of ice in lakes. *Science*, *32*(811), 81–82. https://doi.org/10.1126/science.32.811.81

Blumberg, A. F., & Mellor, G. L. (1987). A description of a three-dimensional coastal ocean circulation model, three-dimensional coastal ocean circulation model. In *Three-dimensional ocean models*. American Geophysical Union. Chapter 4. https://doi.org/10.1029/CO004p0001

Boyce, F. M., Donelan, M. A., Hamblin, P. F., Murthy, C. R., & Simons, T. J. (1989). Thermal structure and circulation in the great lakes. *Atmosphere-Ocean*, *27*(4), 607–642. https://doi.org/10.1080/07055900.1989.9649358

Brown, L. C., & Duguay, C. R. (2010). The response and role of ice cover in lake-climate interactions. *Progress in Physical Geography*, *34*(5), 671–704. https://doi.org/10.1177/0309133310375653

Brown, L. C., & Duguay, C. R. (2011). A comparison of simulated and measured lake ice thickness using a Shallow Water Ice Profiler. *Hydrological Processes*, *25*(19), 2932–2941. https://doi.org/10.1002/hyp.8087

Cai, Y., Ke, C. Q., & Duan, Z. (2017). Monitoring ice variations in Qinghai Lake from 1979 to 2016 using passive microwave remote sensing data. *Science of the Total Environment*, *607–608*, 120–131. https://doi.org/10.1016/j.scitotenv.2017.07.027

Cai, Y., Ke, C. Q., Li, X. G., Zhang, G. Q., Duan, Z., & Lee, H. (2019). Variations of lake ice phenology on the Tibetan Plateau from 2001 to 2017 based on MODIS data. *Journal of Geophysical Research*, *124*(2), 825–843. https://doi.org/10.1029/2018JD028993

Charusombat, U., Fujisaki-Manome, A., Gronewold, A. D., Lofgren, B. M., Anderson, E. J., Blanken, P. D., et al. (2018). Evaluating and improving modeled turbulent heat fluxes across the North American Great Lakes. *Hydrology and Earth System Sciences*, *22*(10), 5559–5578. https://doi.org/10.5194/hess-22-5559-2018

Chatterjee, S., & Hadi, A. S. (1986). Influential observations, high leverage points, and outliers in linear regression. *Statistical Science*, *1*(3), 379–393. https://doi.org/10.1214/ss/1177013622

Chen, C. T. A., & Millero, F. J. (1986). Thermodynamic properties for natural waters covering only the limnological range. *Limnology & Oceanography*, *31*(3), 657–662. https://doi.org/10.4319/lo.1986.31.3.0657

Desai, A. R., Austin, J. A., Bennington, V., & Mckinley, G. A. (2009). Stronger winds over a large lake in response to weakening air-to-lake temperature gradient. *Nature Geoscience*, *2*(12), 855–858. https://doi.org/10.1038/NGEO693

De Silva, L. W. A., Yamaguchi, H., & Ono, J. (2015). Ice–ocean coupled computations for sea-ice prediction to support ice navigation in Arctic sea routes. *Polar Research*, *34*(1), 25008. https://doi.org/10.3402/polar.v34.25008

Fairall, C. W., Bradley, E. F., Grachev, A. A., & Edson, J. B. (2003). Bulk parameterization of air–sea fluxes: Updates and verification for the COARE algorithm. *Journal of Climate*, *16*(4), 571–591. https://doi.org/10.1175/1520-0442(2003)016<0571:BPOASF>2.0.CO;2

Fairall, C. W., Bradley, E. F., Rogers, D. P., Edson, J. B., & Young, G. S. (1996). Bulk parameterization of air-sea fluxes for Tropical ocean-global atmosphere coupled-ocean atmosphere response experiment. *Journal of Geophysical Research*, *101*(C2), 3747–3764. https://doi.org/10.1029/95JC03205

Fujisaki, A., Anderson, E. J., Kessler, J. A., Chu, P. Y., Wang, J., & Gronewold, A. D. (2020). Simulating impacts of precipitation on ice cover and surface water temperature across large lakes. *Journal of Geophysical Research*, *125*(5), e2019JC015950. https://doi.org/10.1029/2019JC015950

Fujisaki, A., Wang, J., Bai, X. Z., Leshkevich, G., & Lofgren, B. (2013). Model-simulated interannual variability of Lake Erie ice cover, circulation, and thermal structure in response to atmospheric forcing, 2003–2012. *Journal of Geophysical Research*, *118*(9), 4286–4304. https://doi.org/10.1002/jgrc.20312

Fujisaki, A., Wang, J., Hu, H. G., Schwab, D. J., Hawley, N., & Rao, Y. R. (2012). A modeling study of ice–water processes for Lake Erie applying coupled ice-circulation models. *Journal of Great Lakes Research*, *38*(4), 585–599. https://doi.org/10.1016/j.jglr.2012.09.021

Gou, P., Ye, Q. H., Che, T., Fang, Q., Ding, B. H., Lin, C. H., & Zong, J. B. (2017). Lake ice phenology of Nam Co, Central Tibetan Plateau, China, derived from multiple MODIS data products. *Journal of Great Lakes Research*, *43*(6), 989–998. https://doi.org/10.1016/j.jglr.2017.08.011

Guo, L. N., Wu, Y. H., Zheng, H. X., Zhang, B., Li, J. S., Zhang, F. S., & Shen, Q. (2018). Uncertainty and variation of remotely sensed lake ice phenology across the Tibetan Plateau. *Remote Sensing*, *10*, 1534. https://doi.org/10.3390/rs10101534

Guo, L. N., Zheng, H. X., Wu, Y. H., Fan, L. X., Wen, M. X., Li, J. S., et al. (2021). An integrated dataset of daily lake surface temperature over Tibetan Plateau [Dataset]. Earth System Science Data, *14*, 3411–3422. https://doi.org/10.5194/essd-2021-151

Guo, L. N., Zheng, H. X., Wu, Y. H., Zhang, T. Q., Wen, M. X., Fan, L. X., & Zhang, B. (2020). Responses of lake ice phenology to climate change at Tibetan Plateau. *Ieee Journal of Selected Topics in Applied Earth Observations and Remote Sensing*, *13*, 3856–3861. https://doi.org/10.1109/JSTARS.2020.3006270

He, J., Yang, K., Tang, W. J., Lu, H., Qin, J., Chen, Y. Y., & Li, X. (2020). Data Descriptor: The first high-resolution meteorological forcing dataset for land process studies over China. [Dataset]. Scientific Data, *7*, 1–11. https://doi.org/10.1038/s41597-020-0369-y

Hibler, W. D. (1979). A dynamic thermodynamic sea ice model. *Journal of Physical Oceanography*, *9*(4), 815–846. https://doi.org/10.1175/1520-0485(1979)009<0815:ADTSIM>2.0.CO;2

Hibler, W. D. (1980). Modeling a variable thickness sea ice cover. *Monthly Weather Review*, *108*(12), 1943–1973. https://doi.org/10.1175/1520-0493(1980)108<1943:MAVTSI>2.0.CO;2

Holland, P. R., & Kay, A. (2003). A review of the physics and ecological implications of the thermal bar circulation. *Limnologica*, *33*(3), 153–162. https://doi.org/10.1016/S0075-9511(03)80011-7

Hook, S. J., Prata, J., Alley, R. E., Abtahi, A., Richards, R. C., Schladow, S. G., & Pálmarsson, G. (2003). Retrieval of lake bulk and skin temperature using along-track scanning radiometer (ATSR-2) data: A case study using Lake Tahoe, California. *Journal of Atmospheric and Oceanic Technology*, *20*(4), 534–548. https://doi.org/10.1175/1520-0426(2003)20<534:ROLBAS>2.0.CO;2

Hsu, S. A. (1988). *Coastal meteorology*. Academic Press Inc.

Huang, A. N., Lazhu, Wang, J. B., Dai, Y. J., Yang, K., Wei, N., et al. (2019). Evaluating and improving the performance of three 1-D lake models in a large deep Lake of the central Tibetan Plateau. *Journal of Geophysical Research*, *124*(6), 3143–3167. https://doi.org/10.1029/2018JD029610

Huang, L., Wang, X. H., Sang, Y. X., Tang, S. C., Jin, L., Yang, H., et al. (2021). Optimizing lake surface water temperature simulations over large lakes in China with Flake model. *Earth and Space Science*, *8*. https://doi.org/10.1029/2021EA001737

Huang, W. F., Zhang, J. R., Leppäranta, M., Li, Z. H., Cheng, B., & Lin, Z. J. (2019). Thermal structure and water-ice heat transfer in a shallow ice-covered thermokarst lake in central Qinghai-Tibet Plateau. *Journal of Hydrology*, *578*, 124122. https://doi.org/10.1016/j.jhydrol.2019.124122

Huang, W. F., Zhao, W., Zhang, C., Leppäranta, M., Li, Z. H., Li, R., & Lin, Z. J. (2021). Radiative penetration dominates the thermal regime and energetics of a shallow ice-covered lake in an arid climate. *The Cryosphere*. https://doi.org/10.5194/tc-2021-349

Hunke, E. C., & Dukowicz, J. K. (1997). An elastic-viscous-plastic model for sea ice dynamics. *Journal of Physical Oceanography*, *27*(9), 1849–1867. https://doi.org/10.1175/1520-0485(1997)027<1849:AEVPMF>2.0.CO;2

Jansen, J., MacIntyre, S., Barrett, D. C., Chin, Y. P., Cortés, A., Forrest, A. L., et al. (2021). Winter limnology: How do hydrodynamics and biogeochemistry shape ecosystems under ice? *Journal of Geophysical Research*, *126*(6), e2020JG006237. https://doi.org/10.1029/2020JG006237

Jonas, T., Terzhevik, A. Y., Mironov, D. V., & Wüest, A. (2003). Radiatively driven convection in an ice-covered lake investigated by using temperature microstructure technique. *Journal of Geophysical Research*, *108*(C6), 3183. https://doi.org/10.1029/2002JC001316

Ke, C. Q., Tao, A. Q., & Jin, X. (2013). Variability in the ice phenology of Nam Co lake in central Tibet from scanning multichannel microwave radiometer and special sensor microwave/imager: 1978 to 2013. *Journal of Applied Remote Sensing*, *7*(1), 073477. https://doi.org/10.1117/1.JRS.7.073477

Ke, L. H., & Song, C. Q. (2014). Remotely sensed surface temperature variation of an inland saline lake over the central Qinghai-Tibet Plateau. *The ISPRS Journal of Photogrammetry and Remote Sensing*, *98*, 157–167. https://doi.org/10.1016/j.isprsjprs.2014.09.007

Kirillin, G., Leppäranta, M., Terzhevik, A., Granin, N., Bernhardt, J. L., Engelhardt, C., et al. (2012). Physics of seasonally ice-covered lakes: A review. *Aquatic Sciences*, *74*(4), 659–682. https://doi.org/10.1007/s00027-012-0279-y

Kirillin, G., Shatwall, T., & Wen, L. J. (2021). Ice-covered lakes of Tibetan Plateau as solar heat collectors. *Geophysical Research Letters*, *48*(14), e2021GL093429. https://doi.org/10.1029/2021GL093429

Kirillin, G., Wen, L. J., & Shatwell, T. (2017). Seasonal thermal regime and climatic trends in lakes of the Tibetan highlands. *Hydrology and Earth System Sciences*, *21*(4), 1895–1909. https://doi.org/10.5194/hess-21-1895-2017

Kraemaer, B. M., Pilla, R. M., Woolway, R. I., Anneville, O., Ban, S., Colom-Montero, W., et al. (2021). Climate change drives widespread shifts in lake thermal habitat. *Nature Climate Change*, *11*(6), 521–529. https://doi.org/10.1038/s41558-021-01060-3

Kropacek, J., Maussion, F., Chen, F., Hoerz, S., & Hochshild, V. (2013). Analysis of ice phenology of lakes on the Tibetan Plateau from MODIS data. *The Cryosphere*, *7*(1), 287–301. https://doi.org/10.5194/tc-7-287-2013

Kumar, L., & Mutanga, O. (2019). Google Earth engine applications [Software]. Remote Sensing, *11*, 591. https://doi.org/10.3390/books978-3-03897-885-5

Lang, J. H., Lyu, S. H., Li, Z. G., Ma, Y. M., & Su, D. S. (2018). An investigation of ice surface albedo and its influence on the high-altitude lakes of the Tibetan Plateau. *Remote Sensing*, *10*(2), 218. https://doi.org/10.3390/rs10020218

Layden, A., MacCallum, S. N., & Merchant, C. J. (2016). Determining lake surface water temperatures worldwide using a tuned one-dimensional lake model (FLake, v1). *Geoscientific Model Development*, *9*(6), 2167–2189. https://doi.org/10.5194/gmd-9-2167-2016

Lazhu, Yang, K., Hou, J. Z., Wang, J. B., Lei, Y. B., Zhu, L. P., et al. (2020). A new finding on the prevalence of rapid water warming during lake ice melting on the Tibetan Plateau. *Scientific Bulletin*, *66*(23), 2358–2361. https://doi.org/10.1016/j.scib.2021.07.022

Leppäranta, M., & Wen, L. J. (2022). Ice phenology in Eurasian lakes over spatial location and altitude. *Water*, *14*(7), 1037. https://doi.org/10.3390/w14071037

Li, R., Lu, Y. Y., Hu, X. M., Guo, D. L., Zhao, P., Wang, N., et al. (2020). Space–time variations of sea ice in Bohai Sea in the winter of 2009-2010 simulated with a coupled ocean and ice model. *Journal of Oceanography*, *77*(2), 243–258. https://doi.org/10.1007/s10872-020-00566-2

Li, Z. G., Ao, Y. H., Lyu, S. H., Lang, J. H., Wen, L. J., Stepanenko, V., et al. (2018). Investigation of the ice surface albedo in the Tibetan Plateau lakes based on the field observation and MODIS products. *Journal of Glaciology*, *64*(245), 1–11. https://doi.org/10.1017/jog.2018.35

Li, Z. G., Lyu, S. H., Ao, Y. H., Wen, L. J., Zhao, L., & Wang, S. Y. (2015). Long-term energy flux and radiation balance observations over Lake Ngoring, Tibetan Plateau. *Atmospheric Research*, *155*, 13–25. https://doi.org/10.1016/j.atmosres.2014.11.019

Lin, Y. C., Fujisaki-Manome, A., & Wang, J. (2022). Recently amplified interannual variability of the Great Lakes ice cover in response to changing teleconnections. *Journal of Climate*, *35*(19), 2683–2700. https://doi.org/10.1175/JCLI-D-21-0448.1

McPhee, M. G., Morison, J. H., & Nilsen, F. (2008). Revisiting heat and salt exchange at the ice-ocean interface: Ocean flux and modeling considerations. *Journal of Geophysical Research*, *113*(C6), C06014. https://doi.org/10.1029/2007JC004383

Mellor, G. L. (1991). An equation of state for numerical models of oceans and estuaries. *Journal of Atmospheric and Oceanic Technology*, *8*(4), 609–611. https://doi.org/10.1175/1520-0426(1991)008<0609:AEOSFN>2.0.CO;2

Mellor, G. L., & Yamada, T. (1982). Development of a turbulence closure model for geophysical fluid problems. *Reviews of Geophysics and Space Physics*, *20*(4), 851–875. https://doi.org/10.1029/RG020i004p00851

Millero, F. J. (1978). *Freezing point of seawater. Annex 6, Eight report of the joint panel on oceanographic tables and standards (JPOTS)* (Vol. 28). UNESCO technical papers in marine sciences.

Mironov, D., Terzhevik, A., Kirillin, G., Jonas, T., Malm, J., & Farmer, D. (2002). Radiatively driven convection in ice-covered lakes: Observations, scaling, and a mixed layer model. *Journal of Geophysical Research*, *107*(C4). https://doi.org/10.1029/2001JC000892

Mortimer, C. H. (1971). Chemical exchanges between sediments and water in the Great Lakes-Speculations on probable regulatory mechanisms. *Limnology & Oceanography*, *16*(2), 387–404. https://doi.org/10.4319/lo.1971.16.2.0387

Mortimer, C. H., & Mackereth, F. J. H. (1958). Convection and its consequences in ice-covered lakes. *Internationale Vereinigung für theoretische und angewandte Limnologie: Verhandlungen*, *13*(2), 923–932. https://doi.org/10.1080/03680770.1956.11895490

Muñoz-Sabater, J. (2019). ERA5-Land hourly data from 1981 to present [Dataset]. Copernicus Climate Change Service (C3S) Climate Data Store (CDS). https://doi.org/10.24381/cds.e2161bac

Ohshima, K. I., & Nihashi, S. (2005). A simplified ice–ocean coupled model for the Antarctic ice melt season. *Journal of Physical Oceanography*, *35*(2), 188–201. https://doi.org/10.1175/JPO-2675.1

Parkinson, C. L., & Washington, W. M. (1979). A large-scale numerical model of sea ice. *Journal of Geophysical Research*, *84*(C1), 311–337. https://doi.org/10.1029/JC084iC01p00311

Qi, M. M., Liu, S. Y., Yao, X. J., Xie, F. M., & Gao, Y. P. (2020). Monitoring the ice phenology of Qinghai Lake from 1980 to 2018 using multi-source remote sensing data and google earth engine. *Remote Sensing*, *12*(14), 2217. https://doi.org/10.3390/rs12142217

Qi, M. M., Yao, X. J., Li, X. F., Duan, H. Y., Gao, Y. P., & Liu, J. (2019). Spatiotemporal characteristics of Qinghai Lake ice phenology between 2000 and 2016. *Journal of Geographical Sciences*, *29*(1), 115–130. https://doi.org/10.1007/s11442-019-1587-0

Qu, B., Kang, S. C., Chen, F., Zhang, Y. J., & Zhang, G. S. (2012). Lake ice and its effect factors in the Nam Co basin, Tibetan Plateau (in Chinese) [Dataset]. Progressus Inquisitiones De Mutatione Climatis, *8*, 327–333. https://doi.org/10.3969/j.issn.1673-1719.2012.05.003

Semtner, A. J. (1976). A model for the thermodynamic growth of sea ice in numerical investigations of climate. *Journal of Physical Oceanography*, *6*(3), 379–389. https://doi.org/10.1175/1520-0485(1976)006<0379:AMFTTG>2.0.CO;2

Smagorinsky, J. (1963). General circulation experiments with the primitive equation. I. The basic experiment. *Monthly Weather Review*, *21*, 99–165. https://doi.org/10.1175/1520-0493(1963)091<0099:GCEWTP>2.3.CO;2

Su, D. S., Hu, X. Q., Wen, L. J., Lyu, S. H., Gao, X. Q., Zhao, L., et al. (2019). Numerical study on the response of the largest lake in China to climate change. *Hydrology and Earth System Sciences*, *23*(4), 2093–2109. https://doi.org/10.5194/hess-23-2093-2019

Su, D. S., Wen, L. J., Gao, X. Q., Leppäranta, M., Song, X. Y., Shi, Q. Q., & Kirillin, G. (2020). Effects of the largest lake of the Tibetan Plateau on the regional climate. *Journal of Geophysical Research*, *125*(22), e2020JD033396. https://doi.org/10.1029/2020JD033396

Subin, Z. M., Riley, W. J., & Mironov, D. (2012). An improved lake model for climate simulations: Model structure, evaluation, and sensitivity analyses in CESM1. *Journal of Advances in Modeling Earth Systems*, *4*(1), M02001. https://doi.org/10.1029/2011MS000072

Sun, L., Liang, X. Z., & Xia, M. (2020). Developing the coupled CWRF-FVCOM modeling system to understand and predict atmosphere-watershed interactions over the Great Lakes region. *Journal of Advances in Modeling Earth Systems*, *12*. https://doi.org/10.1029/2020MS002319

The NCAR Command Language. (2019). The NCAR Command Language (version 6.6.2 [Software]. UCAR/NCAR/CISL/TDD. https://doi.org/10.5065/D6WD3XH5

Thiery, W., Davin, E. L., Seneviratne, S. I., Bedka, K., Lhermitte, S., & Lipzig, N. P. M. (2016). Hazardous thunderstorm intensification over Lake Victoria. *Nature Communications*, *7*(1), 12876. https://doi.org/10.1038/ncomms12786

Thorndike, A. S., Rhthrock, D. A., Maykut, G. A., & Colony, R. (1975). The thickness distribution of sea ice. *Journal of Geophysical Research*, *80*(33), 4501–4513. https://doi.org/10.1029/JC080i033p04501

Tsydenov, B. O., Kay, A., & Starchenko, A. V. (2016). Numerical modeling of the spring thermal bar and pollutant transport in a large lake. *Ocean Modelling*, *104*, 73–83. https://doi.org/10.1016/j.ocemod.2016.05.009

Vermote, E., & Wolfe, R. (2015). MOD09GQ MODIS/Terra surface reflectance daily L2G global 250 m SIN grid V006 [Dataset]. NASA EOSDIS Land Processes DAAC. https://doi.org/10.5067/MODIS/MOD09GQ.006

Wang, J., Bai, X. Z., Hu, H. G., Clites, A., Colton, M., & Lofgren, B. (2012). Temporal and spatial variability of Great Lakes ice cover, 1973-2010. *Journal of Climate*, *25*(4), 1318–1329. https://doi.org/10.1175/2011JCLI4066.1

Wang, J., Hu, H. G., Schwab, D., Leshkevich, G., Beletsky, D., Hawley, N., & Clites, A. (2010). Development of the great lakes ice-circulation model (GLIM): Application to Lake Erie in 2003-2004. *Journal of Great Lakes Research*, *36*(3), 425–436. https://doi.org/10.1016/j.jglr.2010.04.002

Wang, J., Liu, Q. Z., Jin, M. B., Ikeda, M., & Saucier, F. J. (2005). A coupled ice-Ocean Model in the Pan-Arctic and North Atlantic ocean: Simulation of seasonal cycles. *Journal of Oceanography*, *61*(2), 213–233. https://doi.org/10.1007/s10872-005-0033-3

Wang, J. B. (2020). Water temperature observation data at Nam Co lake in Tibet (2011–2014) [Dataset]. National Tibetan Plateau Data Center. https://doi.org/10.11888/Hydro.tpdc.270332

Wang, J. B., Huang, L., Ju, J. T., Daut, G., Ma, Q. F., Zhu, L. P., et al. (2020). Seasonal stratification of a deep, high-altitude, Dimictic Lake: Nam Co, Tibetan Plateau. *Journal of Hydrology*, *584*, 124668. https://doi.org/10.1016/j.jhydrol.2020.124668

Wang, J. B., Huang, L., Ju, J. T., Daut, G., Wang, Y., Ma, Q. F., et al. (2019). Spatial and temporal variations in water temperature in a high-altitude deep dimictic mountain lake (Nam Co), central Tibetan Plateau. *Journal of Great Lakes Research*, *45*(2), 212–223. https://doi.org/10.1016/j.jglr.2018.12.005

Wang, J. B., Zhu, L. P., Daut, G., Ju, J. T., Lin, X., Wang, Y., & Zhen, X. L. (2009). Investigation of bathymetry and water quality of Lake Nam Co, the largest lake on the central Tibetan Plateau. *Limnology*, *10*(2), 149–158. https://doi.org/10.1007/s10201-009-0266-8

Wen, L. J., Lyu, S. H., Kirillin, G., Li, Z. G., & Zhao, L. (2016). Air-lake boundary layer and performance of a simple lake parameterization scheme over the Tibetan highlands. *Tellus A: Dynamic Meteorology and Oceanography*, *68*(1), 31091. https://doi.org/10.3402/tellusa.v68.31091

White, B., Austin, J., & Matsumoto, K. (2012). A three-dimensional model of Lake Superior with ice and biogeochemistry. *Journal of Great Lakes Research*, *38*(1), 61–71. https://doi.org/10.1016/j.jglr.2011.12.006

Woodcock, A. H. (1965). Melt patterns in ice over shallow waters. *Limnol. Oceanor.*, *10*(suppl), 290–297. https://doi.org/10.4319/lo.1965.10.suppl2.r290

Woolway, R. I., Kraemer, B. M., Lenters, J. D., Merchant, C. J., O'Reilly, C. M., & Sharma, S. (2020). Global lake responses to climate change. *Nature Reviews Earth & Environment*, *1*(8), 388–403. https://doi.org/10.1038/s43017-020-0067-5

Woolway, R. I., & Merchant, C. J. (2019). Worldwide alteration of lake mixing regimes in response to climate change. *Nature Geoscience*, *12*(4), 271–276. https://doi.org/10.1038/s41561-019-0322-x

Woolway, R. I., Sharma, S., Weyhenmeyer, G. A., Debolskiy, A., Golub, M., Mercado-Bettínet, D., et al. (2021). Phenological shifts in lake stratification under climate change. *Nature Communications*, *12*(1), 2318. https://doi.org/10.1038/s41467-021-22657-4

Wu, G. J. (2018). Meteorological observation data from the integrated observation and research station of multiple spheres in Namco (2005-2016) [Dataset]. National Tibetan Plateau Data Center. https://doi.org/10.11888/AtmosPhys.tpe.00000049.file

Wu, L. T., Wu, H. D., Li, W. B., Liu, Q. Z., Zhang, Y. F., Liu, Y., & Shan, B. (2005). Sea ice drifts in response to winds and tide in the Bohai Sea (in Chinese). *Acta Oceanologica Sinica*, *27*(5).

Wu, Y., Huang, A. N., Lazhu, Yang, X. Y., Qiu, B., Wen, L. J., et al. (2020). Improvements of the coupled WRF-lake model over Lake Nam Co, central Tibetan plateau. *Climate Dynamics*, *55*(9–10), 2703–2724. https://doi.org/10.1007/s00382-020-05402-3

Wu, Y., Huang, A. N., Lu, Y. Y., Lazhu, Yang, X. Y., Qiu, B., et al. (2021). Numerical study of the thermal structure and circulation in a large and deep dimictic lake over Tibetan Plateau. *Journal of Geophysical Research*, *126*(10), e2021JC017517. https://doi.org/10.1029/2021JC017517

Wu, Y., Huang, A. N., Yang, B., Dong, G. T., Wen, L. J., Lazhu, et al. (2019). Numerical study on the climatic effect of the lake clusters over Tibetan Plateau in summer. *Climate Dynamics*, *53*(9–10), 5215–5236. https://doi.org/10.1007/s00382-019-04856-4

Xue, P. F., Pal, J. S., Ye, X. Y., Lenters, J. D., Huang, C. F., & Chu, P. Y. (2017). Improving the simulation of large lakes in regional climate modeling: Two-way lake–atmosphere coupling with a 3D hydrodynamic model of the Great Lakes. *Journal of Climate*, *30*(5), 1605–1627. https://doi.org/10.1175/JCLI-D-16-0225.1

Xue, P. F., Schwab, D. J., & Hu, S. (2015). An investigation of the thermal response to meteorological forcing in a hydrodynamic model of Lake Superior. *Journal of Geophysical Research*, *120*(7), 5233–5253. https://doi.org/10.1002/2015JC010740

Yan, Y., Gu, W., Xu, Y. J., & Li, Q. (2019). The in situ observation of modelled sea ice drift characteristics in the Bohai Sea. *Acta Oceanologica Sinica*, *38*(3), 17–25. https://doi.org/10.1007/s13131-019-1395-5

Yao, T. D., Thompson, L., Yang, W., Yu, W. S., Gao, Y., Gao, X. J., et al. (2012). Different glacier status with atmospheric circulations in Tibetan Plateau and surroundings. *Nature Climate Change*, *2*(9), 663–667. https://doi.org/10.1038/nclimate1580

Yao, T. D., Xue, Y. K., Chen, D. L., Chen, F. H., Thompson, L., Cui, P., et al. (2019). Recent Third Pole's Rapid warming accompanies cryospheric melt and water cycle intensification and interactions between monsoon and environment: Multidisciplinary approach with observations, modeling, and analysis. *Bulletin America Meteorology Social*, *100*(3), 423–444. https://doi.org/10.1175/BAMS-D-17-0057.1

Yao, X. J., Li, L., Zhao, J., Sun, M. P., Li, J., Gong, P., & An, L. (2016). Spatial-temporal variations of lake ice phenology in the Hoh Xil region from 2000 to 2011. *Journal of Geographical Sciences*, *26*(1), 70–82. https://doi.org/10.1007/s11442-016-1255-6

You, Q. L., Kang, C. H., Li, C. L., Li, M. S., & Liu, J. S. (2007). Variation features of meteorological elements at NamCo station, Tibetan Plateau (in Chinese). *Meteorological Monthly*, *33*(3), 54–60. https://doi.org/10.7519/j.issn.1000-0526.2007.03.008

Yu, Y., Fowler, C., Fetterer, F., & Maslanik, J. (2014). Interannual variability of Arctic landfast ice between 1976 and 2007. *Journal of Climate*, *27*(1), 227–243. https://doi.org/10.1175/JCLI-D-13-00178.1

Zhang, G. Q., Chen, W. F., Zheng, G. X., Xie, H. J., & Shum, C. K. (2020). Are China's water bodies (lakes) underestimated? *Proceedings of the National Academy of Sciences of the United States of America*, *117*(12), 6308–6309. https://doi.org/10.1073/pnas.1922250117

Zhang, G. Q., Luo, W., Chen, W. F., & Zheng, G. X. (2019). The lakes larger than 1km^2 in Tibetan Plateau (v3.1) (1970s-2022) [Dataset]. National Tibetan Plateau/Third Pole Environment Data Center, *64*, 1306–1309. https://doi.org/10.1016/j.scib.2019.07.018

Zhang, G. Q., Yao, T. D., Xie, H. J., Yang, K., Zhu, L. P., Shum, C. K., et al. (2020). Response of Tibetan Plateau lakes to climate change: Trends, patterns, and mechanisms. *Earth-Science Reviews*, *208*, 103269. https://doi.org/10.1016/j.earscirev.2020.103269